Politecnico di Milano

Scuola di Ingegneria Industriale e dell'Informazione

Corso di Laurea Magistrale in Ingegneria Matematica

Theoretical Analysis of Neurovascular Mechanisms Contributing to Retinal Blood Flow Regulation

Tesi di Laurea di:
Alessandra Cardani
Matricola: 816760

Relatore:
Prof. Riccardo Sacco
Correlatori:
Prof.essa Giovanna Guidoboni
Dott. Aurelio G. Mauri

Anno Accademico 2014-2015

Alla mia famiglia

Study hard what interests
you most, in the most
undisciplined, irreverent
and original manner possible
R. P. Feynman

Ringraziamenti

Sono strane le sensazioni che si provano quando si realizza di essere arrivati alla fine di un lungo percorso. Il sollievo e la malinconia si uniscono in un miscuglio agrodolce che riassume la voglia di lanciarsi in nuove sfide e il desiderio di portare con sè i bei momenti passati. Diventa quindi doveroso rivolgere un pensiero alle persone che mi hanno accompagnato fino a questo momento.

Un grande *grazie* va a Riccardo Sacco, Giovanna Guidoboni ed Aurelio Mauri, che in questi mesi intensi mi hanno guidato alla scoperta di un nuovo mondo con passione, non abbandonandomi mai davanti a difficoltà matematiche, numeriche e persino grammaticali.

Il mio più affettuoso pensiero va poi alla mia famiglia che mi ha permesso di arrivare fin qui sostenendomi sempre con grande orgoglio, sia nei momenti buoni che in quelli cattivi. Non so se sarò mai in grado di dimostrarvi appieno la mia graditudine e il mio affetto.

Un *grazie* va anche a Michele che mi è sempre stato accanto senza dubitare mai, non so se io riuscirei ad avere così tanta fiducia in me.

Un pensiero felice va, infine, a tutti gli amici vicini e lontani. In particolare un *grazie* a Erika compagna di viaggio, ansie e sventure. Un ringraziamento ad Alice che mi ha sempre dimostrato che la distanza non può impedire una vera amicizia. Un doveroso pensiero anche a Pasquale, infaticabile aiuto informatico, correttore di bozze e interlocutore durante le mie crisi esistenziali e Luca, insostituibile vicino di banco e compagno di risate. Senza di voi questi anni non sarebbero stati gli stessi. Un ringraziamento anche a tutti gli amici della provincia (tra cui un gran numero di Luca) che mi hanno sempre ricordato che il Poli non è tutto, anche se vorrebbe.

Milano, Dicembre 2015. *Alessandra*

Abstract

The comprehension of blood flow regulatory mechanisms is crucial to understand how degenerative disorders occur and how they can be treated.
Blood flow regulation seems to be based on three main mechanisms: *mechanical regulation*, *metabolic regulation* and *neurovascular coupling*.
In the present thesis we focus on the form of neurovascular coupling that includes feedforward mechanisms that increase blood flow and, consequently, oxygen supply to regions where neurons are particularly active. This regulatory mechanism typically occurs in the brain tissue although it shows up also in other organs of the human body. In particular we focus on the eye retinal tissue because of the experimental evidence that many similarities exists between brain and eye. For example the so-called *blood-brain-barrier* and *blood-retinal-barrier* have not only the same function but also the same structure. The advantage of studying the eye is that several non-invasive techniques exist to investigate ocular dysfunctions.
In this context the use of mathematical modeling may be helpful to interpret and predict experimental data and to test and compare different hypotheses and conjectures.
With this aim in this work we propose and investigate a multiphysic-multiscale mathematical models in order to construct a description of retinal microcirculation that includes the feedforward neurovascular coupling mechanisms. In particular we focus on the role of astrocytes, endothelium cells and smooth muscle cells. Starting from the models presented in [12] and in [16], we devise a novel method to couple the vessel response due to either mechanical stimuli caused by changes in blood flow or vasoactive agents producted by neurovascular coupling mechanisms. Moreover we extend the representative segment model for retinal microcirculation presented in

[2], by including the vasoactive behavior due to the same chemical agents described above. Extensive numerical simulation are conducted to validate the proposed model against realistic baseline conditions and to perform a sensitivity analysis with respect to input data.

Keyword: Blood Flow Regulation, Autoregulation, Retina, Mathematical Model, Neurovascular Coupling, Vascular Response, Astrocyte, Vasomotion, Calcium, EETs, 20-HETE, Nitric Oxide

Sommario

La comprensione dei meccanismi di regolazione del flusso sanguigno è cruciale per capire come si verifichino disordini degenerativi.
Si pensa che la regolazione del flusso sanguigno sia basata su tre meccanismi principali: *meccanico*, *metabolico* e *accoppiamento neurovascolare*.
Il presente lavoro di tesi si concentra sullo studio dell'accoppiamento neurovascolare che comprende un meccanismo di tipo feedforward che aumenta il flusso sanguigno e l'apporto di ossigeno alle regioni con marcata attivita neuronale. Questo meccanismo, tipico del tessuto cerebrale, è presente in molti tessuti. In particolare questa tesi si concentra sul tessuto oculare della retina a causa delle molte somiglianze esistenti tra il cervello e l'occhio. Per esempio le cosiddette *blood-brain-barrier* nel cervello e *blood-retinal-barrier* nell'occhio hanno analoghe funzioni e strutture. Il vantaggio di studiare l'occhio si trova nel gran numero di tecniche non invasive esistenti per lo studio delle disfunzioni oculari.
In questo contesto l'uso di un modello matematico può essere un valido aiuto per interpretare e predire i dati sperimentali, nonchè per testare e confrontare ipotesi e congetture.
Con questo obiettivo in questo lavoro vengono proposti e analizzati alcuni modelli matematici multiscala e multifisici allo scopo di costruire una descrizione per la microcircolazione della retina che includa i meccanismi di accoppiamento neurovascolare. L'attenzione è posta sul ruolo degli astrociti, delle cellule endoteliali e delle cellule muscolari lisce. Partendo dai modelli presentati in [12] e in [16], è stato ideato un metodo per accopiare le risposte del vaso sanguigno dovute a cambiamenti nel flusso sanguigno e all'azione vasoattiva di sostanze prodotte a seguito di attività neuronale. Inoltre è stato esteso il modello semplificato per la microcircolazione nella retina

presentato in [2] includendovi il comportamento vasoattivo dovuto alle sostanze precedentemente analizzate. Sono state svolte umerose simulazioni numeriche per validare il modello proposto rispetto a valori a riposo realistici e per condurre un analisi di sensitività del modello rispetto ai dati in input.

Parole chiave: Regolazione del Flusso Sanguigno, Autoregolazione, Retina, Modello Matematico, Accoppiamento Neurovascolare, Risposta Vascolare, Astrocita, Calcio, EETs, 20-HETE, Ossido Nitrico

Contenuto

Il presente lavoro di tesi è diviso in quattro capitoli:

Il primo capitolo introduce il problema dell'autoregolazione del flusso sanguigno approfondendo aspetti biologici e tecnologici per poi sottolineare l'importanza di un approccio matematico per l'analisi del fenomeno. In particolare si evidenzia la rilevanza dello studio dei meccanismi di regolazione del flusso sanguigno per la comprensione di patologie e terapie innovative. Le più recenti ricerche scientifiche hanno infatti evidenziato come un'inadeguata autoregolazione del flusso sanguigno possa portare a malattie neurodegenerative quali il morbo di Alzheimer, il morbo di Parkinson e il glaucoma. I principali meccanismi di autoregolazione vengono distinti in tre classi principali: *meccanismi meccanici*, *meccanismi metabolici* e *accoppiamento neurovascolare*.

Viene poi dettagliata l'importanza dei meccanismi di autoregolazione nel cervello. In particolare è un fatto ormai riconosciuto che la trasmissione di segnali mediati da neurotrasmettitori, specialmente quelli prodotti dagli astrociti, ha un ruolo chiave nella regolazione del flusso sanguigno. È presentata, inoltre, una panoramica delle principali tecniche di misurazione di parametri d'interesse nel cervello, evidenziando la difficoltà di ottenere dati precisi usando tecniche non invasive.

In seguito si fornisce una breve descrizione delle strutture dell'occhio e di come queste possano essere trattate alla stregua di un *alter ego* delle strutture presenti nel cervello. La somiglianza tra i due organi non si limita alle strutture che li costituiscono ma si estende anche alle patologie da cui essi sono affetti. Molti disturbi neurodegenerativi manifestano infatti sintomi evidenti a carico

dell'occhio. D'altra parte alcuni disturbi tipici dell'occhio (glaucoma) hanno un decorso patologico analogo a quello dei disturbi neurodegenerativi. Viene poi svolta una panoramica delle tecniche di misurazione di parametri d'interesse nell'occhio. Questa evidenzia come l'occhio sia una struttura più accessibile rispetto al cervello: le tecniche sono infatti molto numerose, non invasive e, solitamente, forniscono risultati adeguatamente precisi.

In questo contesto nasce, quindi, l'idea che un modello matematico possa aiutare a trovare risposte alle molteplici domande aperte; analizzando alcune delle difficoltà da affrontare ed evidenziando i numerosi vantaggi che esso potrebbe portare.

Il secondo capitolo introduce a partire da [12, 16] un modello per la descrizione dei fenomeni di neurovascular coupling. In particolare l'attenzione viene posta sul ruolo di tre protagonisti del fenomeno: gli astrociti, le cellule endoteliali e le cellule muscolari lisce. Poiché la caratterizzazione della scala alla quale risolvere il modello risulta non banale a causa della elevata complessità del problema in oggetto, si è scelto di ricondursi a modelli zero-dimensionali, descrivendo i vari fenomeni attraverso equazioni differenziali ordinarie.

Vengono poi presentati i modelli descritti in [12] e [16], analizzando prima le osservazioni biofisiche e sperimentali e poi derivando la formulazione matematica del problema. Viene infine proposto un modello che riassume la descrizione meccanica dei vasi sanguigni proposta in [16] aggiungendovi il meccanismo di accoppiamento neurovascolare analizzato in [12].

Il terzo capitolo si pone l'obiettivo di inserire il meccanismo di accoppiamento neurovascolare precedentemente studiato all'interno di un network di vasi sanguigni. In particolare viene scelto il network della microcircolazione nella retina per i motivi analizzati nel capitolo 1. Quindi viene fornita una breve descrizione del network di vasi nella retina, evidenziandone le particolarità rispetto agli altri organi. Si entra poi nel dettaglio di come agiscano i meccanismi di autoregolazione del flusso sanguigno nella retina, analizzando alcuni

importanti risultati sperimentali.

Viene poi introdotta la descrizione schematica del network usata in [2], analizzandone le principali caratteristiche. È stato, in seguito, possibile aggiungere allo schematismo di [2] il meccanismo studiato nel capitolo 2 attraverso un opportuno upscaling del modello di accoppiamento neurovascolare. Infine, viene proposta una modifica del modello per la microcircolazione della retina accoppiato con il meccanismo neurovascolare al fine di tenere conto dei meccanismi patologici descritti in [24, 22].

Il quarto capitolo contiene i risultati di un'ampia serie di simulazioni numeriche svolte allo scopo di validare e verificare il funzionamento dei modelli descritti nei capitoli 2 e 3. In particolare è stata prestata molta attenzione alla calibrazione dei parametri del modello al fine di poter descrivere efficacemente i meccanismi considerati. I risultati ottenuti mostrano come i modelli riescano a riprodurre i dati sperimentali nonostante le numerose ipotesi semplificative introdotte nella formulazione. Viene posto, infine, l'accento sulle possibili estensioni future dei modelli presentati al fine di ottenere migliori risultati e di inserire ulteriore meccanismi di autoregolazione.

Contents

List of Figures

List of Tables

List of Acronyms

GLU Glutamate 17

EETs epoxyeicosatrienoic acids 17

20-HETE 20-hydroxy-eicosatetraenoic acid 17

mGluRs glutamate receptors 17

IP3 inositol triphosphate 17

ER endoplasmic reticulum 17

SMCs smooth muscle cells 15

NO nitric oxide 28

CRA Central Retinal Artery 37

CRV Central Retinal Vein 38

LA large arterioles 43

SA small arterioles 43

C capillaries 43

SV small venules 43

LV large venules 43

NOS Nitric Oxide Synthase 48

Chapter 1

Blood flow regulatory mechanisms in the brain and in the eye

1.1 Blood flow regulation

The optimal functioning of every organ of our body requires an appropriate and tightly regulated environment. In particular, the correct supply of blood flow, oxygen and metabolic substances is necessary for the maintenance of the structure and function of the organ [26].

Strictly speaking, autoregulation of blood flow in a tissue is the intrinsic ability of a tissue to maintain its blood flow relatively constant despite variations over a large range of pressure. The mechanisms that supervise and control blood flow autoregulation are still unclear. However, it is likely that they rely on a balanced interaction of substances released by the tissue and the vascular endothelium [26]. In a wide sense, blood flow autoregulation can be defined as the capability of an organ to regulate its blood supply in accordance with its needs. This definition implies that blood flow is actively regulated by metabolism through the action of local factors that modulate the tone of the resistance vessels. These factors are released by the vascular endothelium, glial cells and neural tissue surrounding the vessels [26].

The main mechanisms of blood flow regulation can be grouped into three classes [27]:

1. mechanical regulation;
2. metabolic regulation;
3. Neurovascular Coupling (NVC).

In *mechanical regulation* vessels respond to an increased wall tension due to an elevation in intravascular pressure, by constricting their diameter in order to reduce the vessel radius and restore wall tension to a normal level [27]. The contractility of the smooth muscle cells seems to be regulated, in this case, by endothelial cells that respond to chemical agents and mechanical stimuli such as fluid shear stress. When an external force is applied, endothelial cells can release vasoactive agents that change the vessel geometry to minimize the alterations in intracellular stress. Thus, a close coupling exists between mechanics and vascular endothelium [27].
Metabolic regulation results in the adjustment of blood flow during inadequate or excessive nutrient supply, due to either a change in the tissue metabolic activity or a change in flow by virtue of cardiovascular factors. No matter the cause, when tissues are not supplied with the appropriate amount of blood flow, a *feedback mechanism* permits the regulation of the radius of blood vessels in response to increase tissues oxygen demand [27].
The *neurovascular coupling* includes *feedforward mechanisms* that increase blood flow and, consequently, oxygen supply to regions where neurons are particularly active [27, 3]. Active neurons either send a signal directly to blood vessels or activate astrocytes, by glutamate stimulus, to release vasoactive agents into the vessels in order to increase local blood flow. This process is known as *functional hyperaemia* [3].The inhibition of glutamate receptors in the brain reduces *functional hyperaemia*, but does not affect the energy use associated with neuronal activity, providing evidence that metabolic feedback and neurovascular feedforward mechanisms must be distinguished as two different contributors to blood flow regulation in response to neural activity [27].

Figure 1.1: Neuronal activity. Reprinted from [1]

Another interesting problem is to idenfity which vessels exhibit blood flow regulation mechanism. In general, the structures that control blood flow in a particular tissue are the arterioles, which change diameter actively, but there are indications, for example in the brain, that also capillaries could have an active role [27, 3].

1.2 The importance of blood flow regulation in the brain

The human brain comprises only about 2% of the total body mass, and yet it consumes over 20% of the energy produced by the body at rest [3]. This high energy consumption is crucial for the normal functioning of the brain. The energy is mostly used to reverse the ion influxes that underlie synaptic potentials and action potentials (fig: 1.1). If the supply of blood, oxygen and vital substances (e.g. ATP) does not suffice to meet the tissue metabolic demand of the brain, then neurons and glia can get injuried or even die [3]. To sustain neuronal function, the brain needs efficient mechanisms of blood flow regulation, and all the three classes mentioned in section 1.1 are believed to contribute to the optimal performance of the cerebral system.

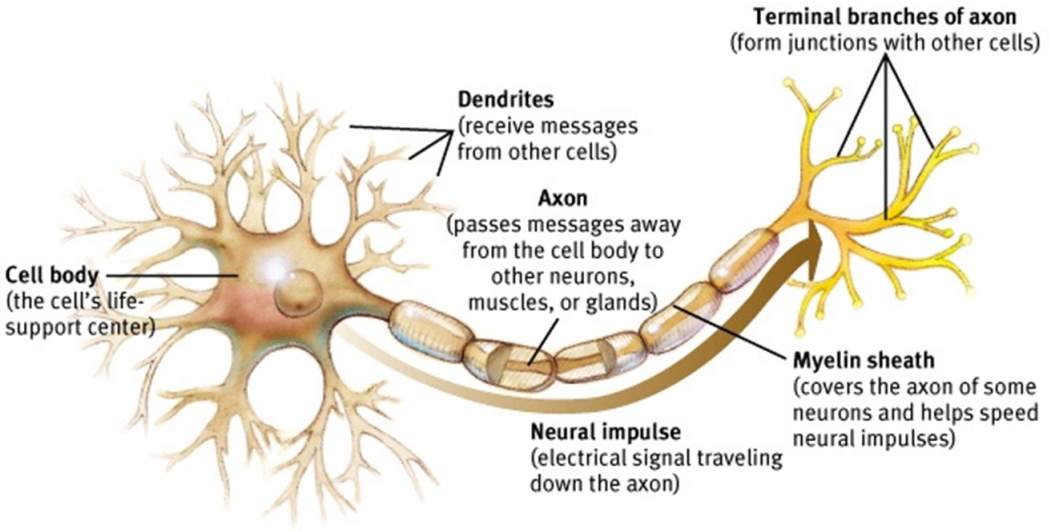

Figure 1.2: Neuronal structure. Reprinted from [4]

Blood flow in the brain seems to be mostly regulated by neurons, astrocytes and endothelial cells. Knowledge of how these cells control blood flow is crucial for understanding how neural computation is powered and for interpreting functional imaging scans. Moreover, understanding the mechanisms that regulate and promote *functional hyperaemia* is a fundamental prerequisite for developing therapies to correct defects in blood flow control that occur in several pathologies such as stroke, hypertension and Alzheimer's desease [3].

It is now recognized that *(i)* neurotransmitter-mediated signalling has a key role in regulating Cerebral Blood Flow (CBF); *(ii)* a large amount of this control is mediated by astrocytes and *(iii)* blood flow may be regulated by capillaries as well as arterioles [3].

Neurons are in general characterized by a central cell body, called soma, that comes in different shapes and is the house of the cell nucleous. Moreover, neurons are viewed as having an input and an output pole. The receiving or input pole typically consists of a large number of branching tree-like extensions of the soma membrane known as dendrites. The dendrites can receive substances and activate the neurons they belong to, in order to transmit a signal to another part of the brain. The output

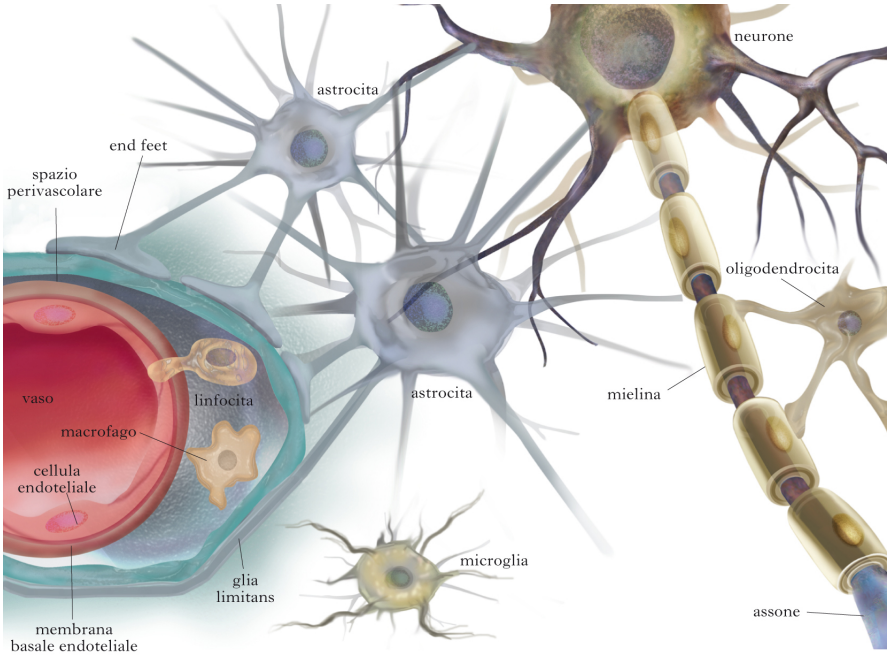

Figure 1.3: Blood vessels, astrocytes, neurons and other glial cells, schematic figure of NVC. Reprinted from [29]

pole, called axon, arises as a single structure from the soma. The axon can conduct electrochemical signals, termed action potentials, away from the soma. At the end of the axon it is likely that some chemical substance or ion go outside the neurons, in the Cerebrospinal Fluid (CSF), permitting the communication with other neurons or different types of cell [21] (fig: 1.2).

Astrocytes surround synapses and thus can be stimulated by neuronal activity, whereas their endfoot processes envelop blood vessels and can send a signal to the smooth muscle cells that control vessel diameter [3] (fig: 1.3).

Endothelial cells in the blood vessels also play a crucial role as they *(i)* separate blood flow from CSF and brain cells forming the so-called "blood brain barrier" and *(ii)* receive substances from neurons, astrocytes, CSF and blood flow, and respond with vasoactive agents actively contributing to blood flow regulation [3].

The relative importance of astrocytes, neurons and endothelial vasodilating pathways remains a matter of debate, mostly because it is difficult to isolate each single pathways in *in vivo* experiments [3].

Despite the above difficulty, it is important to study NVC because this may help understand how degenerative disorders occur and how they can be treated. For example, there is an increasing evidence for vascular factors having a causal role in the development of Alzheimer's disease [17]. Many patients with Alzheimer's disease have regional cerebral hypoperfusion (inadequate blood flow to brain region), which correlates with cognitive decline [17]. Amyloid-β peptide decreases funcional hyperaemia by promoting oxidative stress, which inhibits the production of astrocytic and neuronal vasodilating messengers [17]. Similarly, the formation of an astrocytic scar after traumatic brain injury is likely to profoundly alter neurovascular coupling, thus possibly causing accumulation of Amyloid-β peptide [3].

1.3 Measurement techniques in the brain

A precise measure of brain activity in patients without placing electrodes directly within the brain is very difficult. An overview of the possible non-invasive measurement techniques is provided below.

Functional Magnetic Resonance Imaging (fMRI) uses fluctuations in the magnetic field in the brain to measure changes in CBF volume associated with mental activity. By current standards of blood flow measurement, this technique is quaintly crude, but it points to the idea of investigating neural activity in the brain through changes in local blood flow. One of the main problems with fMRI is that the brain is surrounded by fluid: for a precise measure CSF must remain nearly stable and constant, but brain movements with cardiac pulsation involve shift of CSF [5].

Positron Emission Tomography (PET) is non-invasive, but it does involve exposure to ionizing radiation. PET neuroimaging is based on the assumption that areas of high radioactivity are associated with brain activity. What is actually measured indirectly is blood flow to different parts of the brain, which is, in general, believed to be correlated to brain activity. PET scans are in general superior to all other metabolic imaging methods in terms of resolution and speed of completion, but it is possible to have false results on a PET scan

in particular situations. The biggest drawback of PET scanning is that the radioactivity decays rapidly so PET is limited to monitore short tasks [18].

Transcranial Doppler Ultrasound (TDU) is a non-invasive technique that evaluates blood flow and blood velocity in the brain. A more sophisticated technique, called Transcranial Duplex Ultrasound, combines TDU with real-time ultrasound imaging of the arteries. Images are displayed on a viewing monitor and may also be recorded on film or video for later examination. The main disadvantage of this technique is that additional more invasive tests, such as arteriography of the cerebral blood vessels, are often required to further evaluate abnormal findings and to provide more specific information [11].

Intracranial Pressure (ICP) Monitoring: there exist several techniques to measure ICP, but most of them are invasive; in particular they need to insert sensors in the brain through a hole drilled in the skull [19]. Because of the risks of such an invasive measurement technique, recent researches try to find new ways to estimate ICP. An important example is an ultrasound-based measurement – a two-depth transcranial Doppler (TCD) device – which uses the ophthalmic artery as a natural pressure sensor. This technique seems to be sufficiently accurate and its main advantages are that it is a measurement in absolute ICP units and it can be used in critical situations were an invasive approach is not possible due to the associated risks [28].

1.4 The eye is the window to our soul

Ut imago est animi vultus, sic indices oculi (Cicero [20]).

Philosophers defined the eyes as a window to the soul long before scientists addressed this cliché to determine its scientific basis and clinical relevance. The most recent research has shown many similarities between brain and eye, thus clarifying the importance, in the study of brain processes, of having knowledge on eye anatomy and diseases [17].

During embryonic development, the retina and the optic nerve extend from

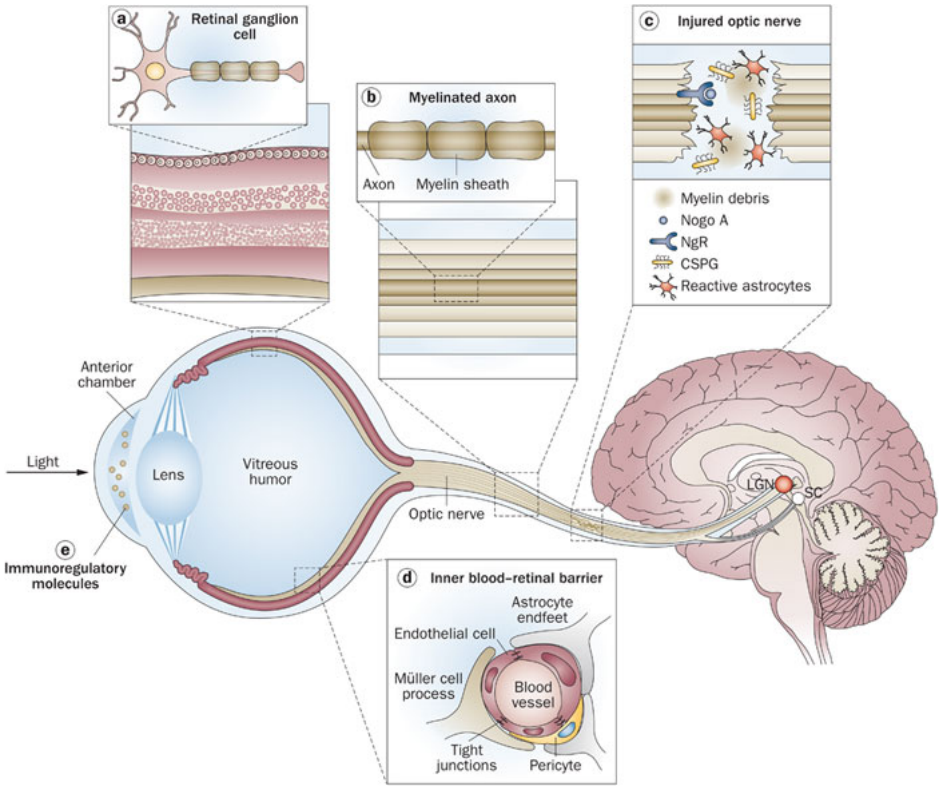

Figure 1.4: Similarity between eye and brain. Reprinted from [17]

the brain, and are thus considered part of the Central Nervous System (CNS) [17]. The retina is composed of layers of specialized neurons that are interconnected through synapses, called retinal ganglion cells, whose axons form the optic nerve. Optic nerve fibers are, in fact, CNS axons. In particular, the optic nerve is the connection between retina and brain and transmits electrical and chemical signals from one organ to the other [17]. The eye is surrounded by an array of blood-ocular barriers that share structure, characteristics and mechanisms with the CNS gating system. For example, the inner blood-retinal barrier is composed of nonfenestrated endothelial cells which are firmly connected by tight junctions and surrounded by astrocytes and Müller cell endfeet, and thus strongly resembles the blood-brain barrier (fig: 1.4). The anterior chamber of the eye is filled with aqueous humour, a fluid that is reminiscent of the CSF circulating around the brain [17].

As the eye is an extension of the brain, it seems reasonable to search for ocular manifestations of brain pathologies [17]. For example in the brain and in the optic

nerve, axonal regeneration after injury is limited. The factors deemed responsibile for the creation of an environment that is nonpermissive for axonal growth are shared between the injured optic nerve and other CNS axons [17]. Indeed, several well-defined neurodegenerative conditions that affect the brain and spinal cord have corresponding manifestation in the eye, and ocular symptoms often precede conventional diagnosis of such CNS disorders. Relevant examples of such pathologies are stroke, Parkinson disease and Alzheimer disease [17]. Dysfunctions of the blood-brain barrier or the blood-retinal barrier are suspected to play a central role in the development of these diseases. More important changes in retinal vascularization can be visualized early in the disease process, and in a direct and noninvasive manner, whereas blood-brain barrier breakdown usually remains undetected until marked vasogenic oedema and brain damage have occurred [17, 23].
Furthermore various eye-specific pathologies share characteristics of neurodegenerative disorders. Such an overlap is probably due to the similarities between the eye and the brain in terms of tissue structure [17]. An important example is Glaucoma: axonal atrophy and deficits in axonal transport preceeding the loss of retinal ganglion cells, trans-synaptic degeneration, and accumulation of amiloid-β in some patient resemble a neurodegenerative disease [17, 23].

The similarity between the eye and the brain makes the eye a valuable model for the study of central nervous system processes in both health and disease. The eye is a convenient research model for several reasons. A first reason is that the eye is relatively easy to access for manipulation and *in vivo* imaging. A second reason is that administration of various compounds to the eye is fairly simple. A third reason is that the optic nerve consists of a long, continuous tract of axons that are uninterrupted by interneurons, which makes it ideally suited for various studies. Finally, as the retina is a well-defined neuronal compartment, it can be isolated in intact form and used to study molecular mechanisms of pathology and reaction to various pharmacological agents [17].
Because of the above mentioned reasons, an increasing scientific effort is currently being devoted to testing whether therapies that are beneficial in brain disorders may

also alleviate eye diseases (and viceversa) [17].

1.5 Measurement techniques in the eye

As described above, many non-invasive measurement techniques exist for the eye. An overview of these techniques is shown below.

Laser Doppler Flowmetry (LDF) is a non-invasive method of assessing blood flow and perfusion in the Optic Nerve Head (ONH). It is based on Doppler effect and utilizes a fundus camera and a computer system to make the computation. LDF can calculate three hemodynamic parameters: velocity, blood volume and blood flow within the ONH. Specifically: velocity is defined as the average speed of red blood cells traveling through capillaries; blood volume is defined as the number of red blood cells in the given sample and blood flux is defined as the flux of red blood cells through a specific part of a capillary at a given time. The main advantage of LDF is its ability to measure three different parameters; however, it only provides measurements of blood perfusion in arbitrary units, which limits its usefulness in a clinical setting. Another problem of this technique is that measurements depend significantly on the depth of the sampled tissue. In fact some studies showed that LDF appears to be more heavily influenced by blood flow changes in the more superficial layer of the ONH than in deeper layers [27].

Optical Coherence Tomography (OCT) angiography is a combination of high speed OCT and a new 3D angiography system called split-spectrum amplitude-decorrelation angiography (SSADA). OCT angiography is a non-invasive method used to estimate blood flow in the ONH, especially within the microcirculation. OCT angiography has many advantages over other types of OCTs: it can visualize the microvasculature, it minimizes the pulsatory bulk motion noise along the axial direction and optimizes flow detection along the transverse direction. One of the main disadvantages of this technique is that blood flow from superficial layers can be projected to deeper layers, thereby incorrectly indicating that the imaged blood flow is a few layers deeper than

its actual location in vivo [27].

Color Doppler Imaging (CDI) is a non-invasive procedure that allows the user to visualize a color-coded image of blood velocity against a gray-scale image of the surrounding structures. It can measure blood flow velocity in absolute units. The major advantages of CDI are that it is non-invasive, vessel selective, reproducible and does not require pupil dilation, clear media or fixation. CDI is limited in its ability to measure only velocity and post-calculate vascular resistance, and requires an experienced operator to obtain accurate results [27].

Laser Speckle Flowgraphy (LSFG) is a non-invasive method of measuring blood flow and velocity in the ONH. The velocity values (calculated through quantitative indicators of blood velocity) are well correlated with blood flow measurements simultaneously taken with other techniques. The distribution of blood flow can be displayed in a two-dimensional color-coded map, which reflects the time variation at each pixel point. This allows for visualization of blood flow in real time. The advantages of LSFG are that its results are adequately reproducible and that the change in velocity at the same site of the same eye can be followed over time. A major disadvantage of LSFG is that the meaning of its measurements is not clearly understood and does not allow for inter-eye or inter-individual comparison [27].

Intraocular Pressure (IOP) Monitoring there are different measurement techniques to estimate IOP, one of the most important being the Goldmann and Perkins Applanation Tonometry. This latter technique is based on the principle that the pressure inside an ideal dry, thin-walled sphere equals the force necessary to flatten its surface divided by the area of flattening. In applanation tonometry, the cornea is flattened and the IOP is determined by varying the applanating force or the area flattened. The main disadvantage of this technique is that measurements are affected by the central corneal thickness and it is now known that a wide variation exists in corneal thickness among individuals [6].

1.6 Virtual lab: a unified model

What is the relative importance of the above mentioned regulating pathways?
What is the quantitative response to an external stimulus?
What are the interactions of the substances involved in the regulating pathways in a complex vessel network?
What are the microscopical mechanisms that lead to a pathological response of the tissue?
These are open questions and answers are not easy to find. As a matter of fact, as described in section 1.5, non-invasive measurement techniques are not sufficiently precise to give us a completly satisfactory answer. On the other hand *in vitro* experiments are not always reliable because cells can change their behavior outside their natural environment.
For this reason a mathematical model could help us to get more information because it is based on fundamental principles and simple chemical reactions. These simple elements can be assembled to describe a complex system. If we would be able to improve a model that can describe the regulation pathways, such a model could be useful to interpret and predict experimental data. Moreover a mathematical model could include some pathologic mechanisms based on experimental hypotheses in order to validate them.

Obviously such a model would be very difficult to construct for many reasons. A first reason is that it is not clear which scale should be used to describe the cells. We could use a model that summarizes the behavior of the entire cell, or it could be relevant to focus on a smaller scale, for example to study the cell membrane. It is fundamental to understand the relative contributions of different model components to the final result and devise a combined description of parts that act together in order to make the computation simpler.
A second reason is that some different cell types have to be described, including neurons, astrocytes, endothelial cells and smooth muscle cells, each one having specific properties and reaction to different input molecules. A possibility is to study each kind of cell separately and describe local cell interaction through suitable interface

conditions. In particular in a spatial simulation (1D, 2D, 3D) the computational domain can be decomposed into different regions for different cells, so that each cell can be studied singularly in a smaller domain that accounts for all cell characteristics. Boundary and interface conditions can interpret the interaction between different domains. For example, in the simulation of an astrocyte in the CSF, we may think of studying the single astrocyte and, separately, the CSF and the interface coupling condition must account for substances that are exchanged from astrocyte and CSF (and viceversa).

A third reason is that it is not a trivial task to reproduce the geometrical and topological structure of the brain, due to the complex structure of blood vessels.

Finally, many models use microscopical input and output parameters, such as resting concentration of some molecules or properties of the pumps distributed on the cell membrane, but the application of such kind of models to the study of real patients, is far from feasible because of the lack of *in vivo*, non invasive, measurements for model calibration. Thus it would be necessary to connect macroscopical measurements to microscopical parameters. Interestingly, we saw that it is easy to quantify many parameters through eye measurements and imaging; so, if we could deduce from these measures the value for microscopical parameters of an individual, we could apply the model without any invasive procedure and predict the state of health of the person. Obviously, another controversial issue is the connection between eye and brain parameters; this is a non trivial matter despite the similarity between the two organs.

Such a multiscale/multiphysics model is not currently available, but if it could be possible to go beyond the above mentioned difficulties, the opportunities will be virtually infinite. For every patient we could measure relevant biophysical parameters with non invasive procedures, and understand if he/she is healthy or in a state of risk for some neurodegenerative disorders, and we could test (without experiments on humans) the response to drugs or pharmacologial agents to search for an appropriate therapy. Obviously, this mathematically-based approach does not replace experimental medical research. Many unknown mechanisms are involved in such a way that it is difficult to ascertain if the response of the model is completely

correct or if any secondary effect has not been considered. Regardelss, the model might provide a very helpful starting point for further investigation.

Chapter 2

Mathematical Modeling of Neurovascular Coupling

Neurovascular coupling (NVC) is the link between neural stimulation and constriction or dilation of the surrounding vasculature. Glial cells mediate this response via their unique anatomy which connects neurons to arterioles [12]. In the present work, we study the model for glial activity proposed in [12] and then we devise a novel method to couple such a model to a mathematical description of vascular response to vasoactive agents.
Our scheme takes into account three cell types with different behavior (see fig: 2.1):

- Astrocytes: they are the most common form of glial cell and are increasingly recognised as modulators of long-term neuronal activity via gliotransmission [12]. They are ideally situated to function as relay cells in neurovascular communication [3]. In fact astrocytes surround synapses and thus can be directly stimulated by neuronal activity, whereas their endfoot processes envelop blood vessels and can transmit signals to the smooth muscle cells (SMCs) that control vessel diameter. Furthermore there is a strong evidence that astrocytes can control blood flow through the production and release of metabolites of Arachidonic Acid (AA) [3].

- Endothelial cells: they are sensitive to mechanical stimuli such fluid shear stress as well as biochemical stimuli. A monolayer of endothelial cells separates

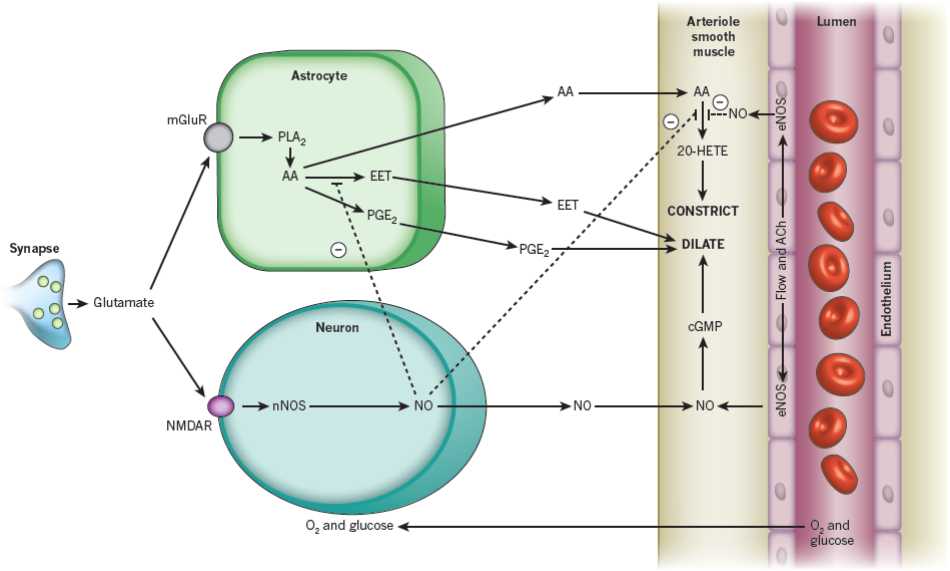

Figure 2.1: Interactions between astrocyte, neuron, endothelium and smooth muscle cells. Reprinted from [3]

the intima (the inner layer of the blood vessel) from the bloodstream. It has become increasingly recognised that this layer is not simply a passive barrier, but plays a crucial role in mantaining vascular homeostasis producing numerous vasoactive factors [25].

- Smooth muscle cells: they are situated around the vessel wall and can contract or relax in response to many substances. Then these cells permit the elastic behavior of the vessel wall and can take into account the "biological" active properties of the vessel responding to chemical stimuli from the other cell types mentioned above [16].

Approaching the mathematical modeling of NVC is not a trivial task, in particular is not easy to use a spatial-dependent description because of the following two reasons:

1. Several scales are involved. A first scale, that we can call *macroscale*, is the vessel scale and it is characterized by the vessel radius and length. A second scale, that we can call *mesoscale*, is the vessel wall scale and it is characterized by the thickness of the tissue around the vessel where diffusion phenomena take place. A third scale, that we can call *microscale*, is the cellular scale and it is characterized by the size of astrocyte, endhotelial and smooth muscle cells.

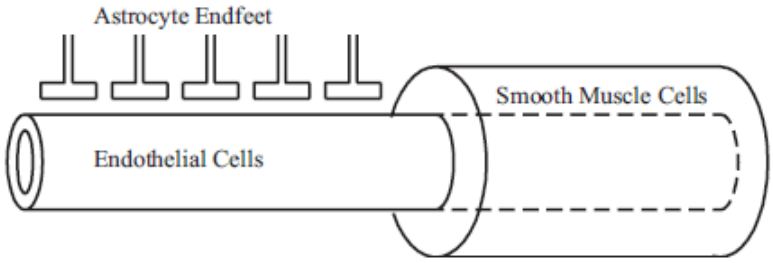

Figure 2.2: Schematic geometry of the vessel surrounded by glial cells. Reprinted from [8]

2. It is not always clear which geometry must be used because the relative position of the cells is not specified in an objective system of reference (see fig: 2.2).

Because of these reasons we decided, to adopt in the present work the approach of reducing the problem to a zero-dimensional context that allows us to use Ordinary Differential Equations (ODEs) to describe the model of NVC.

2.1 Astrocyte Model

In this section we illustrate the main biophysical events that characterize astrocyte activity and then we address their mathematical formulation.

2.1.1 Physiological observation

As we said, there is evidence from brain slice and isolated retina preparation that astrocytes can control blood flow through the production of vasoactive agents [3]. When Glutamate (GLU) is released into the synaptic space from neurons it binds to glutamate receptors (mGluRs) located on the astrocyte surface. This induces release of inositol triphosphate (IP3) into the cytosol. Then IP3 binds to the receptors on the endoplasmic reticulum (ER) (a fundamental intracellular calcium store, see [15]) of astrocytes and this tends to raise cytosolic calcium level (in some cases also long-lasting oscillations in calcium level are observed). In addition AA is released from membrane phospholipidic stores following the increases in cytosolic calcium. The build-up of AA leads to the production os epoxyeicosatrienoic acids (EETs) and 20-hydroxy-eicosatetraenoic acid (20-HETE) which dilate or constrict nearby

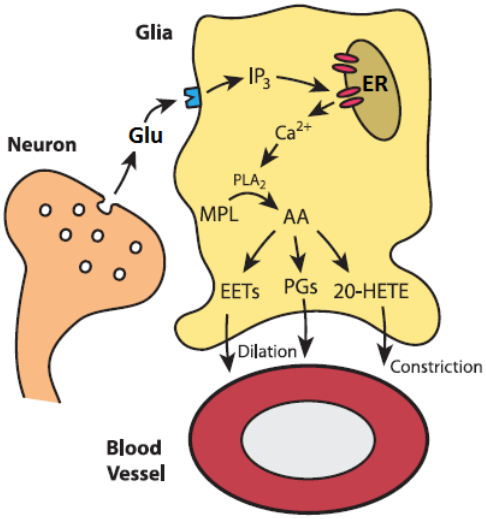

Figure 2.3: Schematic illustration of the mechanisms underlying the production of EETs and 20-HETE. Reprinted from [24]

arterioles respectively (see fig: 2.3).

Despite numerous experimental studies, the specific actions of each vasoactive agent are not yet well characterised. However many studies have successfully reduced or stopped vasomotion by inhibiting either the production of AA or of AA metabolites, this fact implicating the production of AA as a necessary mechanism in neurovascular coupling.

Experimental observation also indicate that vasodilation of neighbouring arterioles follows GLU release with a delay of 1 to 3 s. However, these arterioles return to their baseline diameter on a slower time scale than their initial vasomotive response. Afterwards the hypothesis is that this could be due to a difference in the time scales for the dynamics of EETs ans 20-HETE [12].

2.1.2 Michaelis-Menten description of enzyme kynetics

Before introducing the astrocyte model, let us discuss some results on the analysis of enzyme reactions and how they can be mathematically expressed. These observations are important in view of devising biological models because it is not always possible to have a detailed knowledge for every chemical reaction, but a general scheme can be a good approximation in many cases.

Usually chemical reactions are catalyzed by an enzime. Enzymes help convert other molecules called *substrates* into a product, but they themselves are not changed by the reaction. Enzymes are particularly efficient at speeding up biologial reactions, even up to 10 millions times or more [15].
Enzyme reactions do not follow the law of mass action directly. Indeed as the concentration of substrate ($[S]$) is increased, the rate of the reaction increases only to a certain extent, reaching a maximal reaction velocity at high substrate concentrations. The law of mass action, instead, predicts that the reaction velocity increases linearly as $[S]$ increases.

A model to explain the deviation from the law of mass action was first proposed by Michaelis and Menten [13]. In their reaction scheme, the enzyme E converts the substrate S into the product P through a two-step process. First E combines with S to form a complex C which then breaks down into the product P releasing E in the process. These mechanisms are described by the scheme:

$$S + E \underset{k_{-1}}{\overset{k_1}{\leftrightarrows}} C \overset{k_2}{\rightarrow} P + E \tag{2.1}$$

If we define $s = [S]$, $c = [C]$, $e = [E]$ and $p = [P]$, the law of mass action applied to equation (2.1) yields four differential equations for the rates of change of s, c, e and p:

$$\frac{ds}{dt} = -k_{-1}c - k_1 se \tag{2.2a}$$

$$\frac{de}{dt} = (k_{-1} + k_2)c - k_1 se \tag{2.2b}$$

$$\frac{dc}{dt} = k_1 se - (k_2 + k_{-1})c \tag{2.2c}$$

$$\frac{dp}{dt} = k_2 c \tag{2.2d}$$

Note that, since $\frac{de}{dt} + \frac{dc}{dt} = 0$, the quantity $e + c = e_0$ in conserved, where e_0 is the total amount of available enzyme [15].
Michaelis and Menten assumed that the substrate is at instantaneous equilibrium

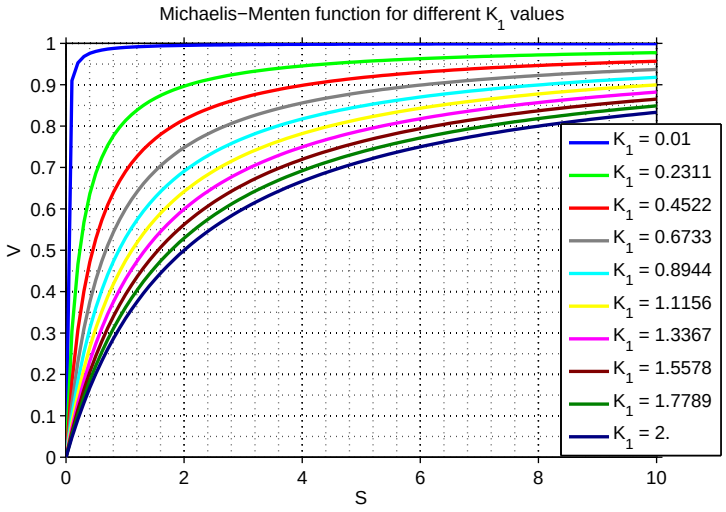

Figure 2.4: Graphical representation of equation (2.5) for $V_{max} = 1$ and different values of K_1

with the complex, and thus:

$$k_1 se = k_{-1} c \tag{2.3}$$

Since $e + c = e_0$ we find that:

$$c = \frac{e_0 s}{K_1 + s} \tag{2.4}$$

where $K_1 = k_{-1}/k_1$. Hence the velocity V of the reaction is given by:

$$V = \frac{dp}{dt} = k_2 c = \frac{V_{max} s}{K_1 + s} \tag{2.5}$$

where V_{max} is the maximum reaction velocity. This latter is attained when all the enzyme is complexed with the substrate.

At small substrate concentrations the reaction rate is linear, whereas at large concentrations the reaction rate saturates to V_{max}, so that the maximum rate of reaction is limited by the amount of enzyme present. At $s = K_1$ the reaction rate is half that of the maximum, therefore we refer hence forth to K_1 as the half saturation constant. In fig: 2.4 some examples of curves obtained for different values of K_1 can be found.

It is important to note that expression (2.3) cannot be exactly correct at all times, but it is only an approximation, in particular it is equivalent to the assumption that $k_{-1} \gg k_2$. However this way of simplifying reactions is used many times in the chemical practice and it is an extremely important technique.

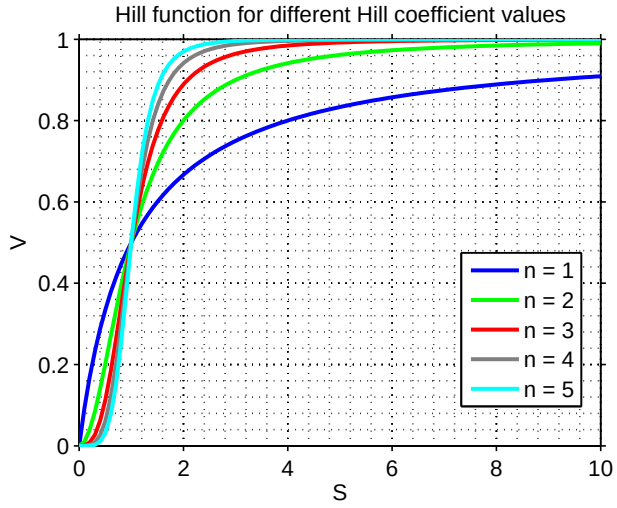

Figure 2.5: Graphical representation of equation (2.6) for $V_{max} = 1$, $K_1 = 1$ and different values of n

Many extensions of equation (2.5) are available to take into account more complex reactions. An example is the Hill equation:

$$V = \frac{V_{max} s^n}{K_1 + s^n} \tag{2.6}$$

where n is the Hill coefficient. In fig: 2.5 some examples of curves obtained for different values of hte Hill coefficient can be found.

2.1.3 Mathematical model

Some models have been proposed to represent the dynamics of the products in astrocytes due to neuronal stimuli (see [12] for an overview). We studied in particular the model proposed in [12] that takes in input the GLU stimuli and, through a cascade of chemical reactions, gives rise to the production of EETs and 20-HETE. A schematic illustration of the model is shown in fig: 2.6.

The main hypotheses of the model, that allow us to use ODEs to describe the system, are:

- the concentration of the substances is homogeneous within the various cell

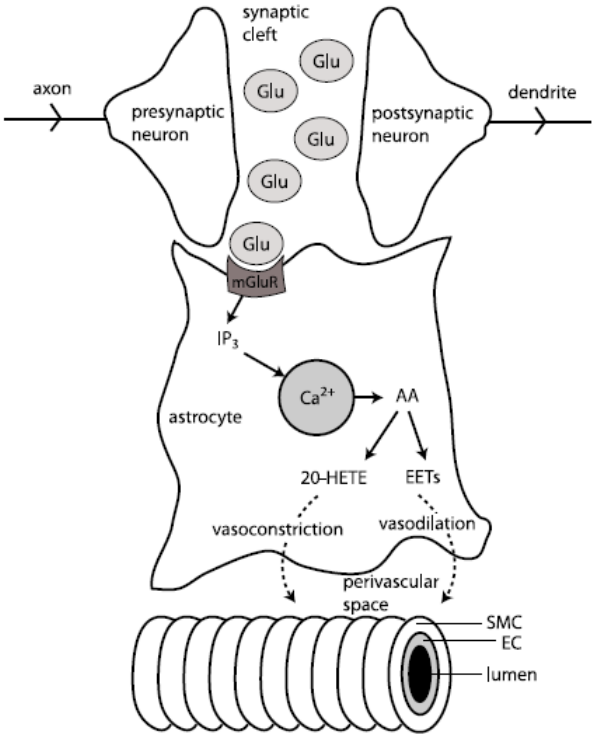

Figure 2.6: Schematic illustration of the model presented in [12]. Reprinted from [12]

compartments, in particular we consider substance concentration in the cytosol or in the ER;

- the astrocyte does not interact with other glial cells in the neighborhood, in particular no calcium fluxes are assumed across the cell membrane (see [12] for a detailed discussion).

The input of the model is the GLU stimulus. The GLU is produced from neuronal activity that is not modelled here. The output of the model is the concentration of EETs and 20-HETE. The other substances that are modelled as mediators from the input to the output are the IP3 concentration, the calcium concentration and the AA concentration.

Let us describe the details of the model.

IP3 Dynamics In the absence of external stimulus IP3 is assumed to decay to a constant baseline concentration with an experimentally determined relaxation time equal to τ_r. The production of IP3 can start in two ways: an external stimulus of GLU or a raise in cytosolic calcium of the cell. The rate of change

of IP3 is hence modeled as:

$$\frac{d[IP_3]}{dt} = J_\delta + J_{glu} - \frac{1}{\tau_r}([IP_3] - [IP_3^*]) \tag{2.7a}$$

$$J_{glu} = \frac{v_g S^p}{k_g^p + S^p} \tag{2.7b}$$

$$J_\delta = v_4 \left(\frac{Ca_i + (1-\alpha)k_4}{Ca_i + k_4} \right) \tag{2.7c}$$

where:

- $[IP_3]$ is the IP3 concentration;
- $[IP_3^*]$ is the baseline concentration;
- J_{glu} is the GLU-induced production of IP3 modelled with an Hill equation because of the complex reactions at the cell membrane;
- J_δ is the calcium-induced production of IP3 modelled with a modified Michaelis-Menten equation;
- S is the GLU concentration;
- Ca_i is the free cytosolic calcium concentration.

The other quantities in system (2.7) are experimentally derived constant (see [12]).

Calcium Dynamics Fluxes across the membrane are considered negligible so that the total amount of calcium in the cell (Ca_t) is constant. There are three possible fluxes between ER and cytosol (see fig: 2.7):

1. flux from ER to cytosol mediated by IP3 ($J_{channel}$) that is driven by the gradient in calcium concentration between ER and cytosol. This flux is regulated by the probability that the channels on ER membrane are open. This probability depends on calcium and IP3 concentrations;
2. a passive leak flux from ER to cytosol (J_{leak}) caused by the difference in calcium concentration between ER and cytosol;
3. an ATP-dependent flux from the cytosol to ER (J_{pump}) initiated by calcium.

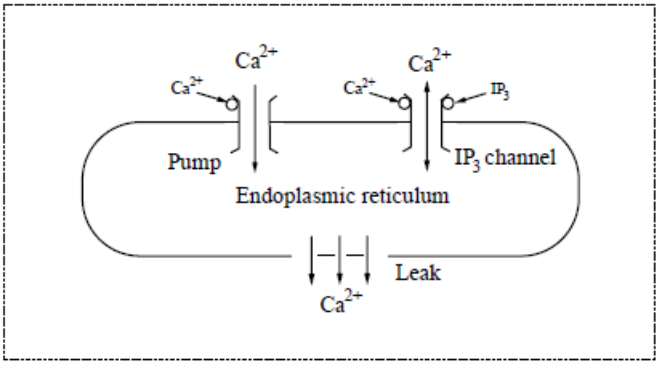

Figure 2.7: Calcium fluxes between cytosol and ER. Reprinted from [9]

These observation lead to the following equation for the cytosolic calcium concentration (Ca_c):

$$\frac{dCa_c}{dt} = J_{channel} + J_{leak} - J_{pump} \tag{2.8}$$

Moreover we must consider that not all cytosolic calcium is free for exchanges, so we must include buffering phenomena. The relationship between free cytosolic calcium (Ca_i) and buffered cytosolic calcium (Ca_b) is experimentally derived and it has the form:

$$Ca_c = Ca_b + Ca_i \tag{2.9a}$$

$$Ca_b = \frac{Ca_i B_T}{Ca_i + K_D} \tag{2.9b}$$

If we define ρ as the fraction of cytosolic calcium that is in the unbuffered form and consider that $K_D \gg Ca_c$ we can write:

$$\rho = \frac{Ca_i}{Ca_c} \cong \frac{K_D}{K_D + B_T} \tag{2.10}$$

Considering equations (2.8), (2.10) and the experimental observation, we obtain the following system of equations for the free cytosolic calcium concentration:

$$\frac{dCa_i}{dt} = \rho(J_{channel} + J_{leak} - J_{pump}) \tag{2.11a}$$

$$J_{channel} = c_1 v_1 m^3 n^3 h^3 (Ca_{ER} - Ca_i) \tag{2.11b}$$

$$J_{leak} = c_1 v_2 (Ca_{ER} - Ca_i) \tag{2.11c}$$

$$J_{pump} = \frac{v_3 Ca_i^2}{Ca_i^2 + k_3^2} \tag{2.11d}$$

$$m = \frac{[IP_3]}{[IP_3] + d_1} \tag{2.11e}$$

$$n = \frac{Ca_i}{Ca_i + d_5} \tag{2.11f}$$

$$\frac{dh}{dt} = \frac{h_\infty - h}{\tau_h} \tag{2.11g}$$

$$h_\infty = \frac{Q2}{Q2 + Ca_i} \tag{2.11h}$$

$$\tau_h = \frac{1}{a_2(Q2 + Ca_i)} \tag{2.11i}$$

$$Q2 = d_2 \left(\frac{[IP_3] + d_1}{[IP_3] + d_3} \right) \tag{2.11j}$$

In system (2.11) the meaning of the symbols is:

- m, n, h are the probabilities that the binding sites of the calcium channels are occupied in such a way that if all sites are occupied the channel is open. m and n act on a faster time scale than h, so that m and n are assumed to be equal to their equilibrium values while h is described with an additional Ordinary Differential Equation (ODE);
- Ca_{ER} is the calcium concentration in ER:

$$Ca_{ER} = \frac{Ca_t + \frac{Ca_i}{\rho}}{c_1}$$

.

The other terms in (2.11) are experimentally derived constants (see [12]).

AA Dynamics AA has a short half life and measuring real-time free AA is difficult so that no quantitative data are available on the AA production rate as a function of calcium concentration. Experimentally, AA production and degradation are assumed to occur instantaneously, so that AA concentration

([AA]) is a calcium-dependent pseudo-steady state in the form $[AA] = f(Ca_i)$. Experimental data show a saturating response of AA to calcium changes [12] so the proposed equation is:

$$[AA] = AA_b + \frac{AA_{max}\Delta Ca_i}{AA_M + \Delta Ca_i} \tag{2.12}$$

where:

- $\Delta Ca_i = Ca_i - Ca^b$ is the increase in calcium concentration with respect to baseline (Ca^b);
- AA_b and AA_{max} are the baseline concentration and maximal increase with respect to the baseline of AA, respectively;
- AA_M is the calcium concentration corresponding to half maximal response.

The values for these parameters are determined experimentally [12]. It is important to observe that $[AA] = AA_b$ when Ca_i is at baseline concentration ($\Delta Ca_i = 0$). If Ca_i increases relation (2.12) predicts an increase of AA above baseline.

20-HETE Dynamics Several experiments highlight the effects of two enzymes (CYP4A11 and CYP4F2) which were responsible for the conversion of AA to 20-HETE. Assuming that the concentrations of the two enzymes are fixed, the production of 20-HETE is modelled by the superposition of two Michaelis-Menten functions and a term of natural degradation:

$$\frac{d[20-HETE]}{dt} = \frac{V_{A11}[AA]}{K_{A11} + [AA]} + \frac{V_{F2}[AA]}{K_{F2} + [AA]} - \lambda[20-HETE] \tag{2.13}$$

where $[20-HETE]$ is the 20-HETE concentration. The other quantities in equation (2.13) are experimentally derived constants (see: [12]).

EETs Dynamics Experimental evidence on the production of EETs is conflicting so that a very simple phenomenological model of relaxation type is assumed

for EETs dynamics:

$$\frac{d[EET]}{dt} = \frac{1}{\tau_{EET}}([EET_\infty] - [EET]) \tag{2.14a}$$

$$EET_\infty = k_{EET}[AA] \tag{2.14b}$$

where $[EET]$ is the EETs concentration and the other terms are experimental constants. Some results suggest that the equilibrium value of EETs is dependent on the concentration of AA and it is the reason of equation (2.14b).

The equations (2.7), (2.9), (2.10), (2.11), (2.12), (2.13) and (2.14) should be solved for the dependent variable $[IP_3](t)$, $Ca_i(t)$, $h(t)$, $[20 - HETE](t)$, $[EET](t)$, for $t \in [0, T_{fin}]$ given $S(t)$ and suitable initial conditions for every variable.

2.2 Vascular model

Analogously to section 2.1, we introduce the basic physiology of the vasculature and then we address its mathematical modeling.

2.2.1 Physiological observation

The arterial wall can be distinguished from an ordinary elastic tube because of two main properties that give a significant contribution to the artery behavior:

1. it is viscoelastic;
2. it is a biological active tube.

The walls of arteries and arterioles contain smooth muscle which can contract or relax in response to nerve impulses and mechanical or chemical stimuli, thereby regulating vessel lumen, blood pressure and flow rate.
In the arterial wall three main layers can be distinguished (see fig: 2.8). The first, inner layer, or *intima*, the middle layer, or *media*, and the outer layer, or *adventitia*. The inner surface of the *intima* is lined with endothelial cells while the *media* containts many SMCs [16].

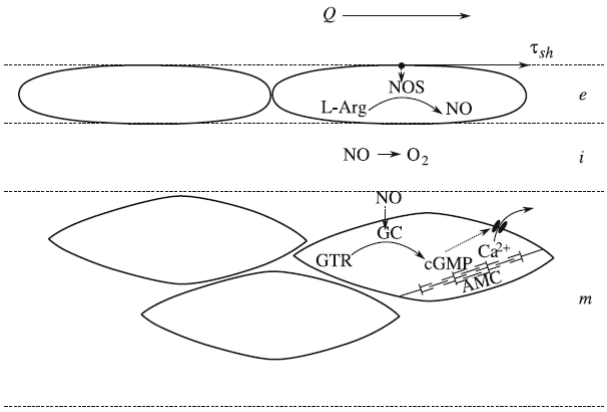

Figure 2.8: Schematic geometry of a vessel. Reprinted from [16]

There are two main mechanisms of local autoregulation. The first mechanism is the muscular tone of the arterial wall due to the shear stress on its inner surface. The second mechanism is determined by the sensitivity of the tissue to the modification of tensile stress by the blood pressure [16]. Hence if the transmural pressure (P_0) is maintained constant then the effects related with shear stress play a main role [16]. It has been shown that an increase in the shear stress at the inner vessel surface leads to the relaxation of the SMCs layer in the arterial wall. This is followed by an increase of artery radius and a consequent decrease in shear stress; therefore the entire process is characterized by the presence of feedback effects [16].

It was long assumed that the endothelial cells lining the inner surface of the arterial bed had the sole role of isolating the blood from the wall tissue, reducing flow friction. However it has been recently shown that the endothelial cell layer plays a key part in the relaxation of the smooth muscles in the artery [16]. Thus, an endothelium-dependent factor in vessel muscle tissue relaxation was discovered. The nitric oxide (NO) was proposed as a signal molecule that connects the endothelium and the SMCs in the artery wall [16]. In particular an increase in the shear stress (τ_{sh}) on the surface of the endothelial cells opens the calcium channels, which leads to an increase in NO. Then NO diffuses with absorption across the layers to the SMCs. NO easy penetrates the membrane of SMCs and stimulates the outflow of intracellular calcium ions. This decrease in intracellular calcium reduces the concentration of the

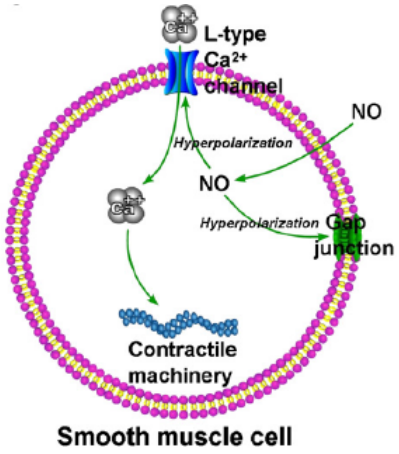

Figure 2.9: Schematic representation of the single SMC behavior. Reprinted from [8]

contracting actin-myosin complexes hence leading to the relaxation of the SMCs (see fig: 2.9 for a schematic representation) [16].

2.2.2 Mathematical model

Following [16], the vascular model undergoes the following main hypotheses:

- axially symmetric and viscoelastic artery;
- blood is assumed to be an incompressible and viscous fluid;
- the flow is assumed to be quasi-stationary;
- the transmural pressure P_0 is constant;
- the radial profile of the axial velocity is assumed to be a power generalization of the Poiseuille law;
- a linear dependence of the muscle force on the phosphorylated myosin concentration in the SMCs is assumed;
- the rate of NO production in the endothelial layer on the inner surface of the arterial wall is assumed to be proportional to the shear stress;

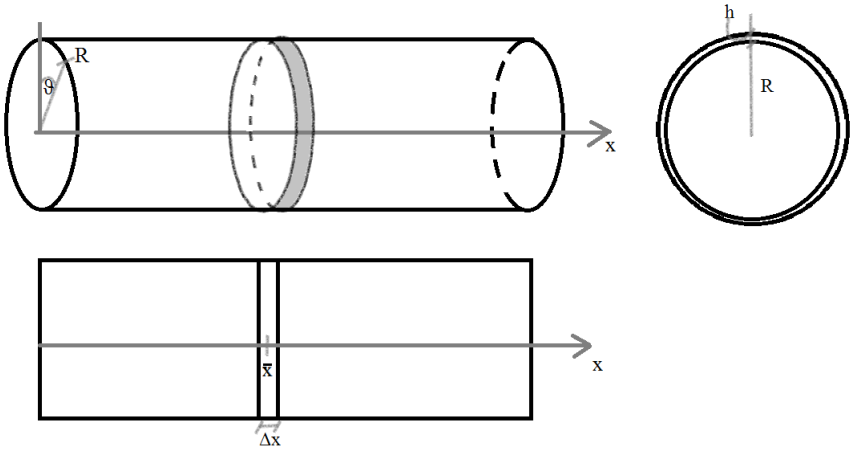

Figure 2.10: Schematic representation of the geometry of the vascular model

- the thickness of the vessel wall h is assumed to be $\ll h_{diff}$ where h_{diff} is the tipical length for the diffusion phenomena in the wall layer. Taking into account typical experimental values $h_{diff} \simeq 100\mu m$ [16]. Thus it is possible to neglect the multilayer structure of the arterial wall and the diffusion of NO and calcium in the various layers;
- the inertia of the wall is neglected.

Let us consider an artery segment of length l and with cross-sectional area A in the cylidrical coordinate system (r, θ, x) (see fig. 2.10). Our model is dependent on the position x only through the velocity profile of the blood in the vessel. Therefore, given the velocity in the position $\bar{x}$, we can focus on an element of small length Δx in the position $\bar{x}$, the dependence of model variables on θ being understood because of axial simmetry.

Description of the shear stress τ_r Let us assume a velocity profile of the form:

$$V_x(r, t; \bar{x}) = \frac{s+2}{s}\left[1 - \left(\frac{r}{R(t;\bar{x})}\right)^s\right] u(t, \bar{x}) \tag{2.15}$$

where:

- V_x is the axial flow velocity component;
- u is the axial velocity component averaged over the cross section;
- R is the internal radius of the artery;

- s is the steepness of the velocity profile.

In the case of a fluid with dynamic viscosity μ, the shear stress can be expressed as:

$$\tau_{sh} = -\mu \left[\frac{\partial V_x}{\partial r}\right]_{r=R} \tag{2.16}$$

Taking into account the flow definition: $Q = Au$ and the above mentioned hypoteses the shear stress τ_{sh} can be written as:

$$\tau_{sh} = \frac{(s+2)\mu}{\pi}\frac{Q}{R^3} = \tau_{sh}^0 \frac{1+\Delta Q}{(1+\eta)^3} \tag{2.17a}$$

$$Q = Q_0(1+\Delta Q(t)) \tag{2.17b}$$

$$R = R_0(1+\eta(t)) \tag{2.17c}$$

$$\tau_{sh}^0 = \frac{(s+2)\mu}{\pi}\frac{Q_0}{R_0^3} \tag{2.17d}$$

Synthesis and Diffusion of NO In the endothelium the production of NO is determined by the shear stress τ_{sh} and is given by:

$$\frac{dn}{dt} = -k_e n + k_3 \tau_{sh} = -k_e n + \frac{\psi_0(1+\Delta Q)}{(1+\eta(t))^3} \tag{2.18a}$$

$$\psi_0 = k_3 \tau_{sh}^0 \tag{2.18b}$$

where:

- n is the NO concentration;
- k_e and k_3 are experimentally determined constants.

For a more complex chemical model we refer to [25].

Calcium Dynamics In deriving the balance equation for the calcium concentration (C) in the SMCs the outward and inward fluxes are taken into account. The first flux is the active transport of calcium from the intracellular space to the extracellular space and generally depends on NO concentration in the SMCs. The second flux is the passive transport of calcium ions through calcium channels, which is determined by the difference between the extracellular calcium

concentration (C_e) and intracellular calcium concentration (C). Because of the thin-wall assumption we can disregard NO diffusion and assume that all the NO product in the endothelium is absorbed from the SMCs leading to the following equation for the intracellular calcium concentration:

$$\frac{dC}{dt} = -\alpha(n)C + \beta(C_e - C) \tag{2.19}$$

Assuming that the dependence of α on the NO concentration is linear and using the fact that $C_e \gg C$, equation (2.19) takes the form:

$$\frac{dC}{dt} = -\alpha_1 C - k_1 n C + \phi_0 \tag{2.20a}$$

$$\alpha(n) = \alpha_1 + k_1 n(t) \tag{2.20b}$$

$$\phi_0 = \beta C_e \tag{2.20c}$$

where the model parameters α_1, k_1 and ϕ_0 are to be determined experimentally.

Active Myosin Dynamics The contraction of SMCs is determined by the activity level of the myosin heads, which depends on the intracellular concentration of calcium ions and on the calcium sensitivity threshold of the specific myosin activating ferments (C_{th}). Two terms should be taken into account in the description of active myosin kinetics. The first term is the natural deactivation of myosin, the second term is the calcium-dependent activation of the actin-myosin complex with a sensitivity threshold to calcium concentration. These two mechanisms lead to the following equation:

$$\frac{df}{dt} = -\alpha_2 f + \gamma(C - C_{th})\mathbf{H}(C - C_{th}) \tag{2.21}$$

where $\mathbf{H}(w)$ is the Heaviside function such that $\mathbf{H}(w) = 1$ for $w \geq 0$ and $\mathbf{H}(w) = 0$ for $w < 0$ while the remaining parameters are experimentally derived constants.

Motion of the Arterial Wall In order to obtain a closed system of ODEs, it is necessary to design a relationship between the artery radius perturbation and

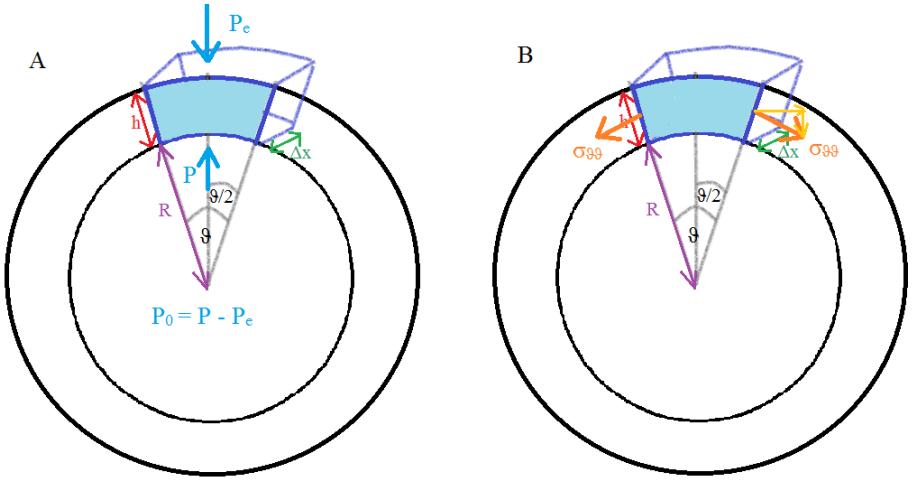

Figure 2.11: Schematic representation of the force acting on a wall element. Panel A: force resulting from transmural pressure applied on the internal face of the vessel. Panel B: force proportional to the tangential stress tensor $\sigma_{\theta\theta}$; the stress is applied on the face of area $h\Delta x$, and then the radial component of $\sigma_{\theta\theta}$ is considered.

the external forces such as the pressure and the muscular force. If we consider a viscoelastic wall element of mass Δm, density ρ_w, thickness h, radius R and length Δx, momentum conservation in radius direction becomes (see fig: 2.11):

$$\Delta m \frac{d^2R}{dt^2} = f_p + f_r \tag{2.22a}$$

$$f_p = P_0 2\pi R \Delta x \tag{2.22b}$$

$$f_r = -2\int_0^{2\pi} \sigma_{\theta\theta} h \Delta x sin(d\theta/2) \simeq -\int_0^{2\pi} \sigma_{\theta\theta} h \Delta x d\theta = -\sigma_{\theta\theta} 2\pi h \Delta x \tag{2.22c}$$

where $\Delta m = \rho_w 2\pi R \Delta x h$, f_p is the force resulting from transmural pression and f_r is proportional to the tangential stress tensor $\sigma_{\theta\theta}$. According to [16] the stress tensor component $\sigma_{\theta\theta}$ consists of three terms: a passive elastic force, the viscous resistance force and the active force due to muscular tone:

$$\sigma_{\theta\theta} = \frac{E(f)}{1-\xi^2}\left[\frac{R-R_0}{R_0} + \kappa_1\left(\frac{R-R_0}{R_0}\right)^2\right] + \lambda\frac{dR}{dt} + k_2 f \tag{2.23}$$

where ξ is Poisson's ratio whereas κ_1 and λ are the nonlinear-elasticity and viscosity coefficients, respectively. Taking into account (2.17c) and the assumption

of neglecting inertia, equation (2.22a) becomes:

$$\lambda h_0 \frac{d\eta}{dt} + \kappa(f)[\eta + \kappa_1 \eta^2] = P_0 - \frac{h_0 k_2}{R_0} f \tag{2.24a}$$

$$\kappa(f) = \kappa_0 \left(1 + \varepsilon \frac{f}{f_0}\right) \tag{2.24b}$$

$$\kappa_0 = \frac{h_0 E_0}{R_0(1-\xi^2)} \tag{2.24c}$$

where the subscript 0 indicates the quantities at the stationary state.

The equation (2.18), (2.20), (2.21) and (2.24) must be solved for $t \in [0, T_{fin}]$ given $\Delta Q(t)$ and suitable initial conditions for each variable in the set (n, C, f, η).

2.3 Neurovascular Coupling Model

The aim of the last model we introduce in this chapter is to reproduce the scheme represented in fig: 2.6. The input is a GLU stimulus that arrives from neuronal activity not modelled yet. Then a cascade of reactions in the astrocyte produces EETs and 20-HETE, the main vasoactive agents products as a feedforward mechanism when neurons are active. These chemical reactions can be described with the model presented in section 2.1. Then we want to focus on an infinitesimal portion of vessel that receives substances from a nearby astrocyte. This vessel responds to mechanical stimuli as in the model presented in section 2.2, but also responds to the vasoactive agents synthesized by the astrocyte.

2.3.1 Mathematical model

The model must couple equations (2.7), (2.9), (2.10), (2.11), (2.12), (2.13) and (2.14) related to the astrocyte model with equations (2.18), (2.20), (2.21) and (2.24) related to the vessel model.

The first consideration is that NVC is a feedforward mechanism, so the vessel dynamics did not change astrocyte behavior. This means that the first group of equations ((2.7), (2.9), (2.10), (2.11), (2.12), (2.13), (2.14)) can be solved offline, given the GLU stimulus.

The hypothesis we use to construct the complete model is that the vasoactive agents EETs and 20-HETE affect the calcium dynamics, similarly to NO. Therefore, the equation (2.19) can be generalized as:

$$\frac{dC}{dt} = -\alpha^n(n)C - \alpha^E([EET])C + \alpha^H([20-HETE])C + \beta(C_e - C) \tag{2.25}$$

Under the assumption of linear dependence of α^n, α^E, α^H on the NO, EETs and 20-HETE concentrations, respectively, and using the fact that $C_e \gg C$, equation (2.25) becomes:

$$\frac{dC}{dt} = -\tilde{\alpha}_1 C - k_1^n n C - k_1^E [EET]C + k_1^H [20-HETE]C + \phi_0 \tag{2.26a}$$

$$\alpha^n(n) = \alpha_1^n + k_1^n n(t) \tag{2.26b}$$

$$\alpha^E([EET]) = \alpha_1^E + k_1^E [EET](t) \tag{2.26c}$$

$$\alpha^H([20-HETE]) = \alpha_1^H + k_1^H [20-HETE](t) \tag{2.26d}$$

$$\tilde{\alpha}_1 = \tilde{\alpha}_1^n + \alpha_1^E - \alpha_1^H \tag{2.26e}$$

$$\phi_0 = \beta C_e \tag{2.26f}$$

Therefore the complete NVC model reads:

For $t \in [0, T_{fin}]$, given $S(t)$, $\Delta Q(t)$ and suitable initial conditions for $[IP_3]$, Ca_i, h, $[20-HETE]$, $[EET]$, n, C, f and η, solve:

$$\frac{d[IP_3]}{dt} = J_\delta + J_{glu} - \frac{1}{\tau_r}([IP_3] - [IP_3^*]) \tag{2.27a}$$

$$J_{glu} = \frac{v_g S^p}{k_g^p + S^p} \tag{2.27b}$$

$$J_\delta = v_4 \left(\frac{Ca_i + (1-\alpha)k_4}{Ca_i + k_4} \right) \tag{2.27c}$$

$$\frac{dCa_i}{dt} = \rho(J_{channel} + J_{leak} - J_{pump}) \tag{2.27d}$$

$$J_{channel} = c_1 v_1 m^3 n^3 h^3 (Ca_{ER} - Ca_i) \tag{2.27e}$$

$$J_{leak} = c_1 v_2 (Ca_{ER} - Ca_i) \tag{2.27f}$$

$$J_{pump} = \frac{v_3 Ca_i^2}{Ca_i^2 + k_3^2} \tag{2.27g}$$

$$m = \frac{[IP_3]}{[IP_3] + d_1} \tag{2.27h}$$

$$n = \frac{Ca_i}{Ca_i + d_5} \tag{2.27i}$$

$$\frac{dh}{dt} = \frac{h_\infty - h}{\tau_h} \tag{2.27j}$$

$$h_\infty = \frac{Q2}{Q2 + Ca_i} \tag{2.27k}$$

$$\tau_h = \frac{1}{a_2(Q2 + Ca_i)} \tag{2.27l}$$

$$Q2 = d_2 \left(\frac{[IP_3] + d_1}{[IP_3] + d_3} \right) \tag{2.27m}$$

$$[AA] = AA_b + \frac{AA_{max} \Delta Ca_i}{AA_M + \Delta Ca_i} \tag{2.27n}$$

$$\Delta Ca_i = Ca_i - Ca^b \tag{2.27o}$$

$$\frac{d[20-HETE]}{dt} = \frac{V_{A11}[AA]}{K_{A11} + [AA]} + \frac{V_{F2}[AA]}{K_{F2} + [AA]} - \lambda[20-HETE] \tag{2.27p}$$

$$\frac{d[EET]}{dt} = \frac{1}{\tau_{EET}}([EET_\infty] - [EET]) \tag{2.27q}$$

$$EET_\infty = k_{EET}[AA] \tag{2.27r}$$

$$\frac{dn}{dt} = -k_e n + \frac{\psi_0(1 + \Delta Q)}{(1 + \eta(t))^3} \tag{2.27s}$$

$$\frac{dC}{dt} = -\tilde{\alpha}_1 C - k_1^n n C - k_1^E [EET] C + k_1^H [20-HETE] C + \phi_0 \tag{2.27t}$$

$$\frac{df}{dt} = -\alpha_2 f + \gamma(C - C_{th})\mathbf{H}(C - C_{th}) \tag{2.27u}$$

$$\lambda h_0 \frac{d\eta}{dt} + \kappa(f)[\eta + \kappa_1 \eta^2] = P_0 - \frac{h_0 k_2}{R_0} f \tag{2.27v}$$

$$\kappa(f) = \kappa_0 \left(1 + \varepsilon \frac{f}{f_0} \right) \tag{2.27w}$$

where all the parameters are defined above and are experimentally derived constants.

Chapter 3

Retinal Microcirculation

The knowledge of mechanisms underlying the pathophysiology of the retinal microcirculation has a fundamental clinical importance since glaucoma and ischemic microangiopathies of the inner retina are the most common cause of blindness in developed countries [26, 23]. Impairment of retinal circulation results in blood flow alterations that, in turn, affect the delivery of oxygen and metabolic substances necessary for the maintenance of retinal structure and function [26]. Thus a mathematical model could serve an interesting virtual lab where different mechanisms can be investigated.

3.1 Anatomy of retinal circulation

The delivery of metabolic substances and oxygen to the retina in mammals is accomplished by two separate vascular systems, namely, the retinal and the choroidal system [26](see fig:3.1). Retinal photoreceptors have the highest cellular metabolic rate in the human body. The metabolic needs of the photoreceptors are satisfied by the choroidal vasculature. The more modest metabolic demands of the neurons and glial cells of the inner portions of the retina are met by the retinal vasculature [24]. Autoregulation mechanisms are present in the retinal circulation, but are less developed in choroidal vessels [24] so that we focus on retinal microcirculation.

The blood supply to the retina is secured by the Central Retinal Artery (CRA),

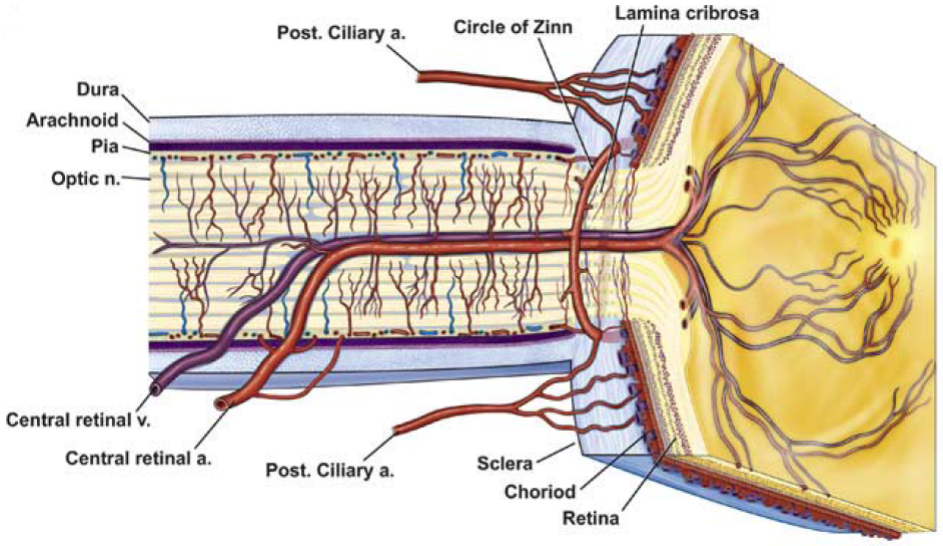

Figure 3.1: Anatomy of the ocular circulation. Cut away drawing of the human eye along the superior–inferior axis through the optic nerve, showing the vascular supply to the retina and choroid. The retinal vessels are supplied by the central retinal artery and central retinal vein. Drawings by Dave Schumick from Anand-Apte and Hollyfield, reprinted from [24]

which emerges through the lamina cribrosa at the optic disk, where it divides into two major branches (fig:3.1). These in turn divide into arterioles extending outward from the optic disk, each supplying one quadrant of the retina. The retinal arterioles give rise to a plexus of capillaries supplying horizontal cells, bipolar cells, amacrine cells and Müller glial cells (see fig: 3.4). The venous system of the retina has a similar arrangement with the Central Retinal Vein (CRV) leaving the eye through the optic disk to drain venous blood into the cavernous sinus [26, 24].
The largest vessels lay in the innermost portion of the retina, close to the inner limiting membrane, whereas the capillaries lie in an interconnecting network that is arranged in a basic two-layered pattern. The first capillary layer is located in the nerve fiber and ganglion cell layer, and the second one lies deeper in the inner nuclear layer (fig: 3.2). The capillary walls are in close spatial relationship with glial cells, mainly astrocytes [26].

The so-called *blood-retinal-barrier* separates blood flow and retinal glial cells. Cellular barriers separate functional compartments, maintain their homeostasis and control transport between them. Barrier tissues are highly dynamic structures and

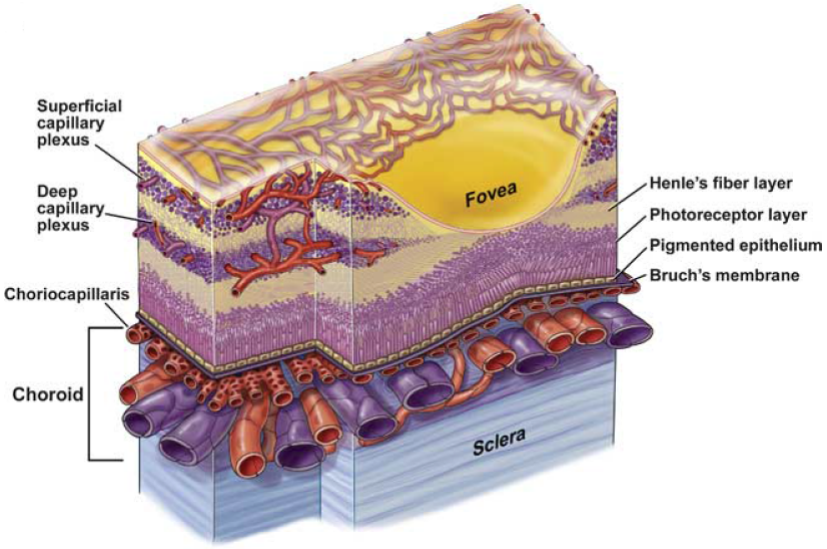

Figure 3.2: Anatomy of the ocular circulation. Drawing showing the vasculature of the retina and choroid. Retinal arterioles and venules lie on the vitreal surface of the retina while capillary plexi lie just beneath the surface and in the inner nuclear layer. Drawings by Dave Schumick from Anand-Apte and Hollyfield, reprinted from [24]

are capable to rapidly respond to physiological requirements as well as to changes in extrinsic conditions [26]. This extreme efficiency in responding to various stimuli is achieved by different cell types. In particular retinal arteries have an unusually developed smooth muscle layer, which makes them different from arteries of the same size in other organs. In humans, the walls of the largest retinal arterioles, close to the optic disk, comprise five to seven layers of smooth muscle cells. After several branchings of the vascular network, the number of muscle layers diminishes to just one or two in the retinal periphery. Moreover, the smooth muscle cells are oriented both circularly and longitudinally in order to permit a precise modulation of the blood flow (see fig: 3.3) [26]. Furthermore, endothelium is considered one of the main components of the inner blood-retinal barrier. In fact endothelial cells are oriented longitudinally along the axis of the vessel and share their basement membrane with adjacent smooth muscle cells and pericytes [26]. Thanks to its position, the endothelium releases a number of metabolic factors, such as NO, that contribute to the blood flow autoregulation. Another important cell type of the blood-retinal-barrier is the pericyte. Pericytes provide structural support to the vasculature. Moreover it seems that they are able to regulate the capillary diameter

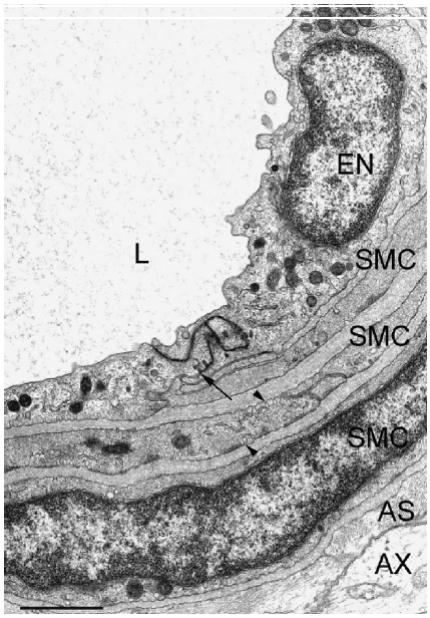

Figure 3.3: Inner blood-retinal barrier. Electron micrograph of an artery in the inner pig retina. The vessel wall is composed of the endothelium (EN) and three layers of smooth muscle cells (SMCs), with numerous caveolae (arrowheads). Astrocytic processes (AS) enwrap the vessel; axon (AX). Reprinted from [26]

and modulate barrier permeability. Finally, glial cells surround the vessels and provide signals that have an impact on the maintenance of the barrier (see fig: 3.5) [26].

3.2 Autoregulation of retinal blood flow

Autoregulation is present in the retinal circulation and functional hyperaemia is well developed in the retinal vasculature [24]. It is believed that the ability to regulate blood flow is crucial for proper retinal function because of its high metabolic activity [26]. In particular, with increased neuronal activity in the retina, there is a need for enhanced oxygen and glucose supply and removal of metabolites. The increase in retinal blood flow serves this need. Moreover the loss of functional hyperaemia that occurs in certain diseases may compromise retinal health and may contribute to the development of pathologies [24].

Studies on the effect of dark and light adaptation on retinal hemodynamics have reported rather controversial results. Luminance flicker seems to induce changes

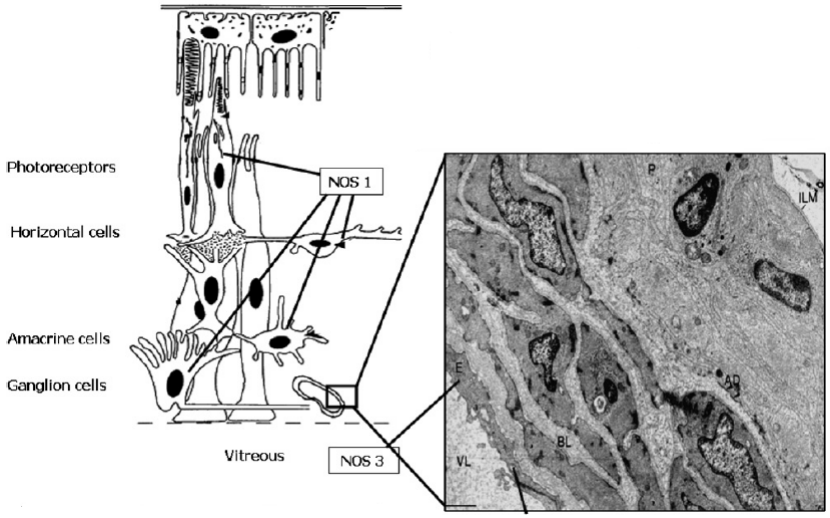

Figure 3.4: Schematic representation of the cell layers in the retina. Reprinted from [26]

in retinal vessel diameter and retinal blood flow [26]. Several studies report that a flickering stimulus dilates the primary arterioles on the retinal surface, leading to an increase in blood flow in arterioles, capillaries and venules of the retina and optic disk [24]. This increase in blood flow in the largest arterioles supplies active neurons in the inner and middle retinal layers by increasing oxygen and glucose. On the other hand, the blood flow increase in the capillaries of the optic disk supplies the active axons of the retinal ganglion cells [24]. Nevertheless, the characteristics of this hyperaemic response such as the temporal dynamics and magnitude depend on stimulus characteristics such as flicker frequency and luminance [26]. Thus, experimental data suggest a coupling between the flicker-induced blood flow changes and the changes in neural activity, underlining the importance of NVC mechanisms. Both feedforward signals as well as metabolic negative feedback signals may contribute to functional hyperaemia in the retina. As a matter of fact, light-evoked vasodilation and vasocontriction are blocked when neuron-to-glia signaling is interrupted, suggesting the importance of the feedforward mechanism. It seems that EETs and 20-HETE produced by glial cells play a central role in vasomotion [26]. Some results suggest that also NO plays a central role in NVC, partially exerting its effect by modulating glial regulation of the vasomotor response [22].

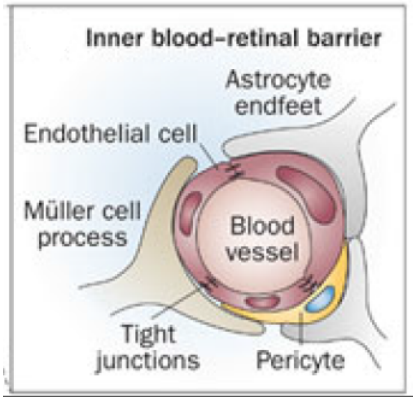

Figure 3.5: Schematic representation of blood-retinal barrier. Reprinted from [17]

3.3 Schematic representation of retinal microcirculation

The rate of retinal blood flow depends on the interaction of various factors which determine the perfusion pressure, i.e. the pressure that drives blood into the retinal vascular system, and the vascular resistance generated by the retinal vessels and the blood viscosity [26].

For an incompressible homogeneous viscous liquid (with viscosity μ) flowing through a cylindrical tube of length L with constant circular cross-section of radius R, the Hagen-Poiseuille law can be applied. Then using an hydraulic analogy to Ohm's law where blood flow is equivalent to current flowing in a resistance, we have:

$$Res = \frac{128L\mu}{\pi(2R)^4} \tag{3.1a}$$

$$Q = \frac{\Delta P}{Res} \tag{3.1b}$$

where ΔP represents the pressure difference between the two ends of the tube [2, 10].

Application of equation (3.1) to a microvascular bed is, however, complicated by many factors, including the dependence of viscosity on local hematocrit, shear rate, changes in the velocity profile of the red blood cells and rheological factors relating to vessel branching. In particular the resistance of a blood vessel depends upon its diameter, its length and the viscosity of the blood. In the retinal vasculature bed,

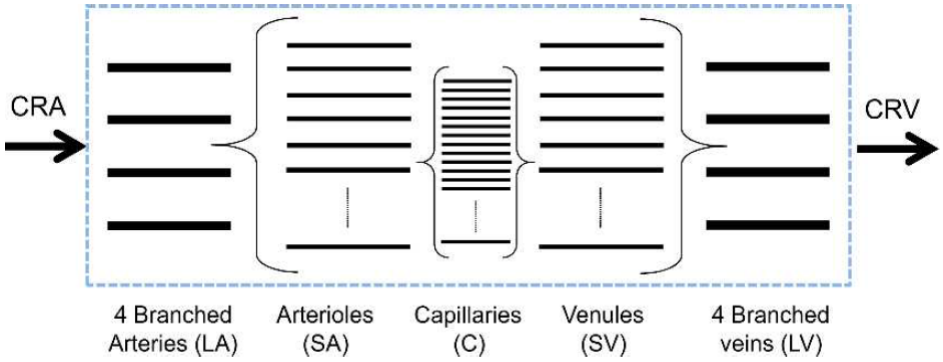

Figure 3.6: Representative segment model. The retinal vasculature is represented by five compartments downstream of the central retinal artery (CRA) and upstream of the central retinal vein (CRV). The blue dotted line indicates the compartments considered in this model. The vessels in the LA and SA compartments are assumed to be vasoactive, and the remaining compartments are fixed resistances. Reprinted from [2]

changes in vessel length are not considered to play a major role in the regulation of blood flow [26]. The diameter of the retinal resistance vessels is modulated by the interaction of multiple systemic factors and local control mechanisms affecting the smooth muscle cells, such as NVC [26]. Blood viscosity is related to hematocrit, but in some experimental settings it seems to be almost constant [26]. Thus the resistance can be computed using constant L and μ if the radius is known.

A simplified model, known as a *representative segment model*, can be used to describe retinal microcirculation [2, 10]. The vasculature can be divided into five main compartments connected in series and containing a set of identical, parallel-arranged segments that experience the same hemodynamic conditions, as shown in figure 3.6. The downstream flow of the CRA can be studied through five representative segments: large arterioles (LA), small arterioles (SA), capillaries (C), small venules (SV), large venules (LV). The pathway is assumed to be symmetric with respect to the vessel length (L) and number (N) in corresponding arteriolar and venous compartments. Furthermore, the LA and SA are assumed to be vasoactive and the remaining compartments are considered to be fixed resistances [2]. Capacitors are added to take into account the ability of blood vessels to mechanically deform and store blood volume in correspondance of a given difference between pressure inside and outside

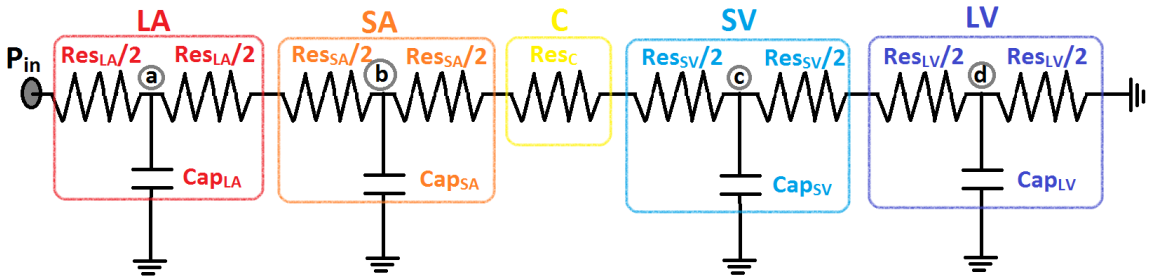

Figure 3.7: Equivalent circuit for retinal microcirculation

the compartment [10]. The resultant equivalent circuit is represented in figure 3.7. The capacitance values are experimentally derived [10] while resistance values are:

$$Res_i = \frac{128 L_i \mu_i}{\pi N_i (2R_i)^4} \qquad i = LA, SA, C, SV, LV. \tag{3.2}$$

Thus the blood flow in the CRA becomes:

$$Q_{CRA} = \frac{P_{in} - P_a}{Res_{LA}/2}. \tag{3.3}$$

Therefore, if the resistance and capacitance values are known, the Kirchhoff current laws at nodes a, b, c and d of the circuit are:

$$Cap_{LA}\frac{dP_a}{dt} + \frac{P_a}{Res_1} + \frac{P_a - P_b}{Res_1 + Res_2} + = \frac{P_{in}}{Res_1} \tag{3.4a}$$

$$Cap_{SA}\frac{dP_b}{dt} + \frac{P_b - P_c}{Res_2 + Res_C + Res_3} + \frac{P_b}{Res_1 + Res_2} - \frac{P_a}{Res_1 + Res_2} = 0 \tag{3.4b}$$

$$Cap_{SV}\frac{dP_c}{dt} + \frac{P_c - P_d}{Res_3 + Res_4} + \frac{P_c}{Res_2 + Res_C + Res_3} - \frac{P_b}{Res_2 + Res_C + Res_3} = 0 \tag{3.4c}$$

$$Cap_{LV}\frac{dP_d}{dt} + \frac{P_d}{Res_4} + \frac{P_d}{Res_3 + Res_4} - \frac{P_c}{Res_3 + Res_4} = 0 \tag{3.4d}$$

where $Res_{LA}/2 = Res_1$, $Res_{SA}/2 = Res_2$, $Res_{SV}/2 = Res_3$ and $Res_{LV}/2 = Res_4$.

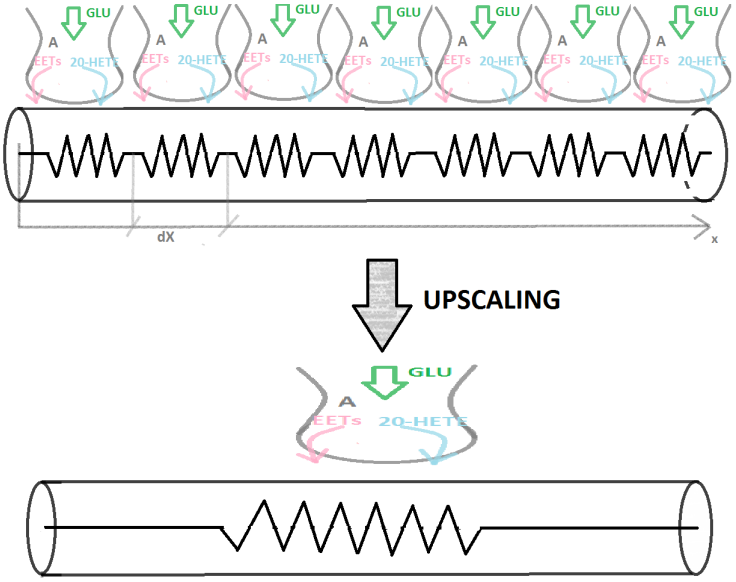

Figure 3.8: Schematic representation of the upscaling procedure that is used to connect the NVC and the network models

3.4 Neurovascular coupling model for retinal microcirculation

To calculate the values of the resistances in model (3.4), we need to determine the values of vessel radii. First of all there are experimental values of the radii for the equilibrium state [2]. Nevertheless the LA and SA vessels are vasoactive and we want to include in the mathematical description the NVC mechanisms studied in chapter 2.

The main problem is that the approaches in section 2.3.1 and 3.3 are basically different: the NVC model is a local model that studies the radius variation in an infinitesimal portion of the vessel, whereas the network model is a macroscale model that assumes that the radius is uniform in all the vessel length. Thus an upscaling of the NVC model is in order. With this aim, we suppose that all the tissue around the vessel is active and we use a single GLU input which corresponds to an average value. From this input we apply the NVC model to calculate the radius variation in the vessel. Then we suppose that the radius is uniform for all the vessel length so that the computed radius corresponds to an average value (see figure 3.8). This hypothesis is coherent with experimental results [22].

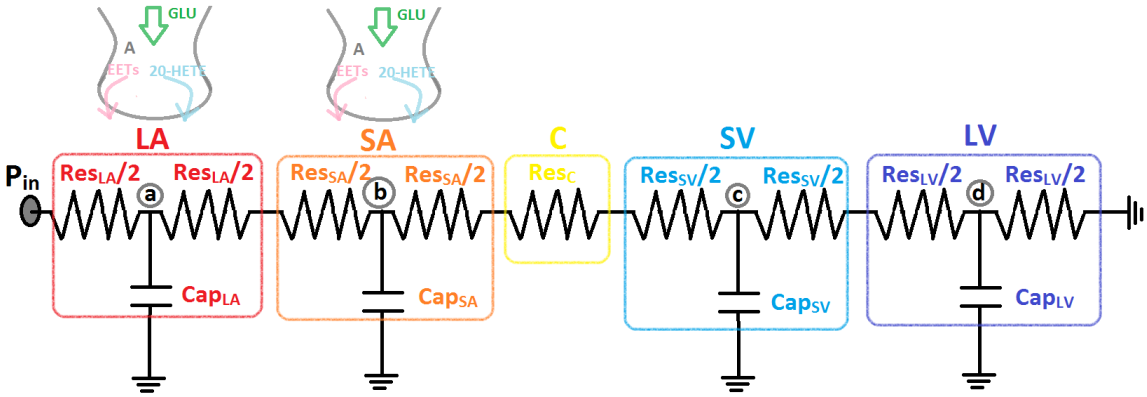

Figure 3.9: Schematic representation of the model for neurovascular coupling in retinal microcirculation

Another hypothesis to simplify the connection between the NVC and network models is that all the vessels of a single compartment receive the same GLU input, so we can use a single resistance calculated as in eq (3.2) instead of a parallel of many different resistances. A scheme of the final model is represented in figure 3.9.

Finally the equations for the complete model reads as follows:

For $t \in [0, T_{fin}]$ given:

$S^{(m)}(t)$, $m = LA, SA$, $P_{in}(t)$ and suitable initial conditions for $[IP_3]^{(m)}$, $Ca_i^{(m)}$, $[20-HETE]^{(m)}$, $[EET]^{(m)}$, $n^{(m)}$, $C^{(m)}$, $f^{(m)}$, $\eta^{(m)}$, P_a, P_b, P_c and P_d, $m = LA, SA$, solve:

for $m = LA, SA$:

$$\frac{d[IP_3]^{(m)}}{dt} = J_\delta^{(m)} + J_{glu}^{(m)} - \frac{1}{\tau_r}([IP_3]^{(m)} - [IP_3^*]) \tag{3.5a}$$

$$\frac{dCa_i^{(m)}}{dt} = \rho(J_{channel}^{(m)} + J_{leak}^{(m)} - J_{pump}^{(m)}) \tag{3.5b}$$

$$[AA]^{(m)} = AA_b + \frac{AA_{max}\Delta Ca_i^{(m)}}{AA_M + \Delta Ca_i^{(m)}} \tag{3.5c}$$

$$\frac{d[20-HETE]^{(m)}}{dt} = \frac{V_{A11}[AA]^{(m)}}{K_{A11} + [AA]^{(m)}} + \frac{V_{F2}[AA]^{(m)}}{K_{F2} + [AA]^{(m)}} - \lambda[20-HETE]^{(m)} \tag{3.5d}$$

$$\frac{d[EET]^{(m)}}{dt} = \frac{1}{\tau_{EET}}([EET_\infty]^{(m)} - [EET]^{(m)}) \tag{3.5e}$$

$$\frac{dn^{(m)}}{dt} = -k_e n^{(m)} + \frac{\psi_0^{(m)}(1+\Delta Q)}{(1+\eta^{(m)}(t))^3} \tag{3.5f}$$

$$\frac{dC^{(m)}}{dt} = -\tilde{\alpha}_1 C^{(m)} - k_1^n n^{(m)} C^{(m)} - k_1^E [EET]^{(m)} C^{(m)} + k_1^H [20-HETE]^{(m)} C^{(m)} + \phi_0^{(m)} \tag{3.5g}$$

$$\frac{df^{(m)}}{dt} = -\alpha_2 f^{(m)} + \gamma(C^{(m)} - C_{th})\mathbf{H}(C^{(m)} - C_{th}) \tag{3.5h}$$

$$\lambda h_0^{(m)} \frac{d\eta^{(m)}}{dt} + \kappa(f^{(m)})[\eta^{(m)} + \kappa_1 \eta^{(m)2}] = P_0^{(m)} - \frac{h_0^{(m)} k_2}{R_0^{(m)}} f^{(m)} \tag{3.5i}$$

$$R^{(m)} = R_0^{(m)}(1+\eta^{(m)}) \tag{3.5j}$$

$$Res^{(m)} = \frac{128 L^{(m)} \mu^{(m)}}{\pi N^{(m)} (2R^{(m)})^4} \tag{3.5k}$$

$$Cap_{LA}\frac{dP_a}{dt} + \frac{P_a}{Res_1} + \frac{P_a - P_b}{Res_1 + Res_2} + = \frac{P_{in}}{Res_1} \tag{3.5l}$$

$$Cap_{SA}\frac{dP_b}{dt} + \frac{P_b - P_c}{Res_2 + Res_C + Res_3} + \frac{P_b}{Res_1 + Res_2} - \frac{P_a}{Res_1 + Res_2} = 0 \tag{3.5m}$$

$$Cap_{SV}\frac{dP_c}{dt} + \frac{P_c - P_d}{Res_3 + Res_4} + \frac{P_c}{Res_2 + Res_C + Res_3} - \frac{P_b}{Res_2 + Res_C + Res_3} = 0 \tag{3.5n}$$

$$Cap_{LV}\frac{dP_d}{dt} + \frac{P_d}{Res_4} + \frac{P_d}{Res_3 + Res_4} - \frac{P_c}{Res_3 + Res_4} = 0 \tag{3.5o}$$

$$Q_{CRA} = \frac{P_{in} - P_a}{Res_{LA}/2} \tag{3.5p}$$

$$\Delta Q = \frac{Q_{CRA} - Q_{0CRA}}{Q_{0CRA}} \tag{3.5q}$$

where Q_{0CRA} is the steady state value for Q_{CRA} when $S^{(m)} = 0$ for $m = LA, SA$; J_δ, J_{glu}, $J_{channel}$, J_{leak}, J_{pump}, ΔCa_i, $[EET_\infty]$ and $\kappa(f)$ are defined in system (2.27) for $m = LA, SA$. Res_1, Res_2, and all the parameters are defined in sections 2.3.1 and 3.3.

3.5 An example on the introduction of pathological conditions

Model (3.5) can be used to study pathological conditions by including mechanisms that are supposed to play a key role in the considered disease and to test if it

is possible to reproduce the experimental results.

For example NO plays a complex role in vasomotor activity; in diabetic retinopathy, increased levels of NO seem to be responsible for suppressing flicker-evoked vasodilation [24].
NO is produced not only by endothelium cells, but also by neurons. A principal effect of NO is to dilate vessels acting on calcium level in vascular smooth muscle cells [22]. In both humans and cats, systemic administration of non-selective Nitric Oxide Synthase (NOS) inhibitors at neuronal level reduces flicker-evoked increases in blood flow. These results seem to support NO as an important mediator of NVC [24]. However additional studies indicate that the effects of NO are more involved [24]. In the ex vivo rat retina, inhibition of neural NOS results in an increase, rather than a decrease, in flicker-evoked vasodilation. Moreover, when NO levels are raised by adding NO donors, a flicker-evoked vasoconstrictions occurs. Thus the hypothesis is that the principal effect of neural NO in the retina may be as a modulator of neurovascular coupling, not as a mediator [24]. The mechanism by which NO suppresses flicker-evoked vasodilation is not known. However, the modulatory effect of NO could be due to its inhibition of EETs production. With less EETs being produced, vasodilation is expected to be smaller and vasoconstriction to be unmasked [24]. A representation of the supposed mechanism can be found in figure 2.1.

Therefore, if we want to include the modulating action of NO in our model, we must consider the following mechanisms and assumptions:

1. neural NO level must be fixed
2. when neural NO is at baseline level, the behavior of the system should be the same as in healthy condition;
3. a fraction of neural NO is absorbed by astrocytes and it inhibits EETs production;
4. a fraction of neural NO is absorbed by SMCs and it acts as a vasodilator agent.

A simple way to proceed is to fix the neural NO level ($[nNO]$) as an input. Moreover $[nNO]$ must satisfy:

$$[nNO] = \delta[nNO] + (1 - \delta)[nNO] \tag{3.6}$$

where δ is the NO fraction absorbed by the astrocyte. A more complex expression than (3.6) could be used to take into account, for example, a portion of NO that survives in the CSF or in the vitreous humor.

Moreover equation (2.14) should be changed to take into account the different EETs production:

$$\frac{d[EET]}{dt} = \frac{1}{\tau_{EET}} \left([EET_\infty] - \left(1 + \beta\delta \frac{[nNO] - [nNO]_b}{[nNO]_b} \right) [EET] \right) \tag{3.7}$$

where $[nNO]_b$ is the baseline value of $[nNO]$ in the healthy state and β expresses the effective modulatory behavior of $[nNO]$.

Finally the calcium equation in SMCs (2.26a) should be changed into:

$$\frac{dC}{dt} = -\tilde{\alpha}_1 C - k_1^n (n + (1-\delta)([nNO] - [nNO]_b)) C - k_1^E [EET] C + k_1^H [20 - HETE] C + \phi_0 \tag{3.8}$$

This is the simplest behavior that could be modelled according to the hypotheses based on experimental data. Should simulation fail to explain data results, it is likely that more complex expressions have to be used for equations (3.6), (3.7) and (3.8) or that some further (unknown) mechanisms are presently being neclected.

Chapter 4

Numerical Results

In this chapter we show an extensive series of numerical results on the models described in chapter 2 and 3. The analysis of conducted simulations will allow to highlight the potentiality of mathematical modeling in biology, as well as the advantages and disadvantages of the presented formulation to better understand the possibility of future extensions.

4.1 Astrocyte model

The model presented in section 2.1.3 has been solved using the parameter values indicated in [12] and reported in table 4.1.
The baseline condition is defined as the steady state with no glutamate application, and it is used to set the initial condition for the model variables in the subsequent simulations. Due to the difficulties in solving analitically equations (2.7), (2.9), (2.10), (2.11), (2.12), (2.13) and (2.14) at equilibrium, the baseline values are determined by solving the system numerically.
The astrocyte model is used here to investigate the following three mechanisms:

1. Calcium oscillations: long-lasting calcium oscillations are reported in several experiments [12]. As a matter of fact, calcium oscillations are a well-known signaling mechanism based on neural stimulation [12].

2. Time scale: the experimental hypothesis is that EETs and 20-HETE act on different time scales. The model should be able to capture this difference in

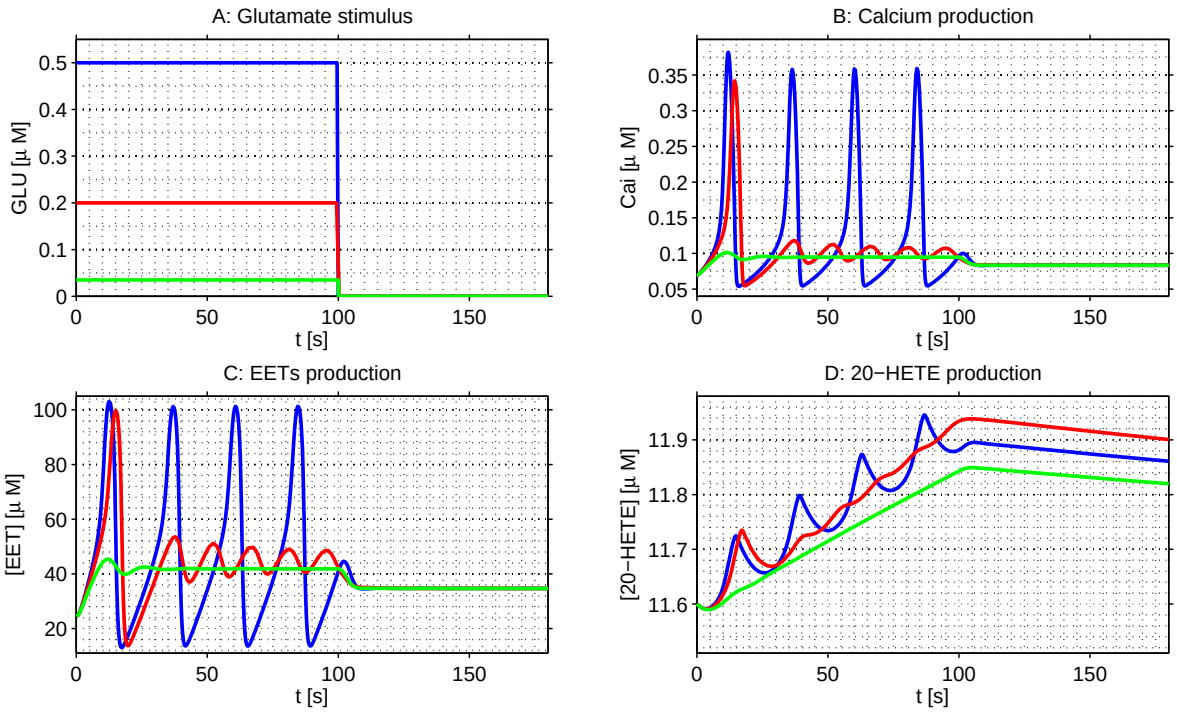

Figure 4.1: Response of an astrocyte to different glutamate stimuli. The blue line represents the response to the stimulus $S = 0.5\mu M$ for $t < 100s$, the red line represents the response to the stimulus $S = 0.2\mu M$ for $t < 100s$, the green line represents the response to stimulus $S = 0.035\mu M$ for $t < 100s$. The glutamate concentration (panel A), the calcium concentration (panel B), the EETs concentration (panel C) and the 20-HETE concentration (panel D) are shown.

time scale in order to reproduce correctly the vasodilating pathway.

3. Neural stimuli: a realistic form for the GLU input is not available. Thus, theoretical profiles with different amplitudes are considered.

Figure 4.1 compares the results obtained by adopting three different step functions to describe the glutamate stimulus. All the three functions have the same time duration ($100s$), but different maximum values (S); in particular, we consider a strong stimulus with $S = 0.5\mu M$ for $t < 100s$ (blue line), a moderate stimulus with $S = 0.2\mu M$ for $t < 100s$ (red line) and a weak stimulus with $S = 0.035\mu M$ for $t < 100s$ (green line). High glutamate levels lead to sustained calcium oscillations, whereas low glutamate levels lead to a decay in calcium oscillations towards an equilibrium value above the baseline. Interestingly, the dynamics of the two vasoactive agents can be easily identified thanks to their different time scales. The

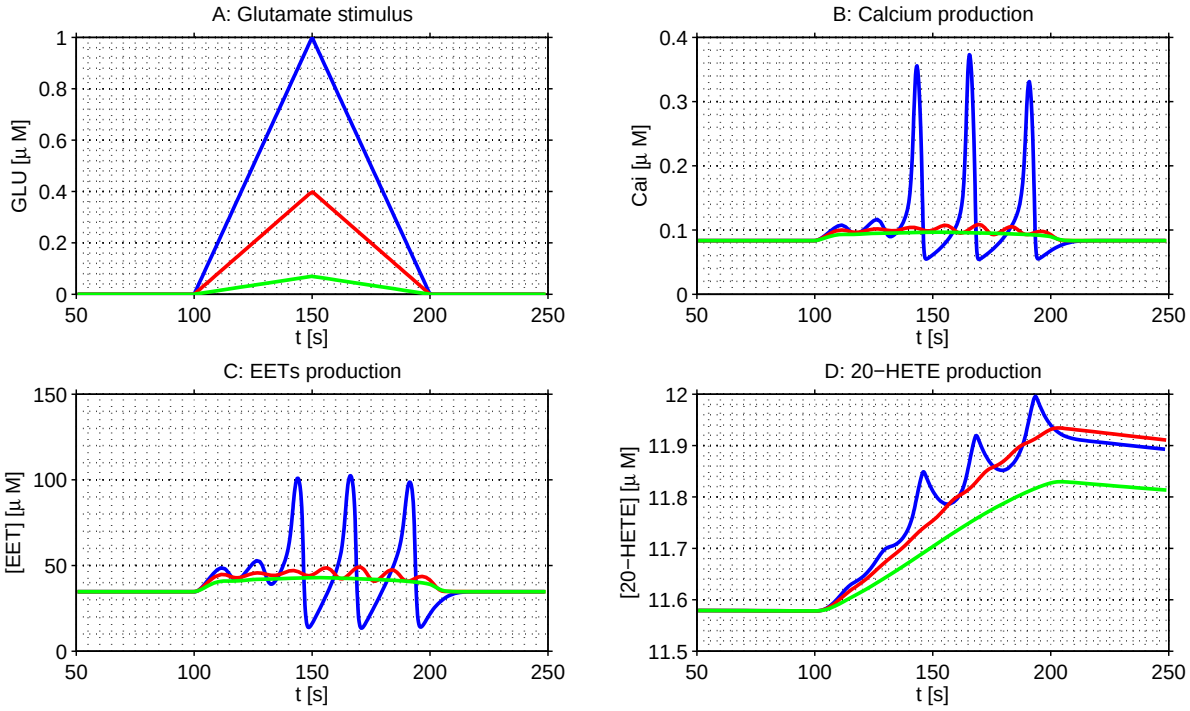

Figure 4.2: Response of an astrocyte to different triangular glutamate stimuli. The blue line represents the response to the stimulus with peak $S = 1\mu M$, the red line represents the response to the stimulus with peak $S = 0.4\mu M$, the green line represents the response to the stimulus with peak $S = 0.07\mu M$. The glutamate concentration (panel A), the calcium concentration (panel B), the EETs concentration (panel C) and the 20-HETE concentration (panel D) are shown.

vasodilator EETs rapidly approaches either a steady state (at low GLU levels) or a sustained oscillatory state (at high GLU levels). In contrast, the concentration of the vasoconstrictor 20-HETE exhibits an increasing trend while the stimulus is active. The 20-HETE necessitates a substantially longer time to achieve a steady state than the characteristic time for vasomotion. Hence, the effects of the vasodilator dominate in the period immediately following the onset of glutamate. Furthermore, EETs returns to its baseline concentration on a much faster time scale than 20-HETE. Hence, the effects of the vasoconstrictor dominate in the period subsequent to the removal of the GLU stimulus.

Figure 4.2 compares the results obtained by applying three different triangular glutamate stimuli for the same observational time of $250s$, reaching different peak

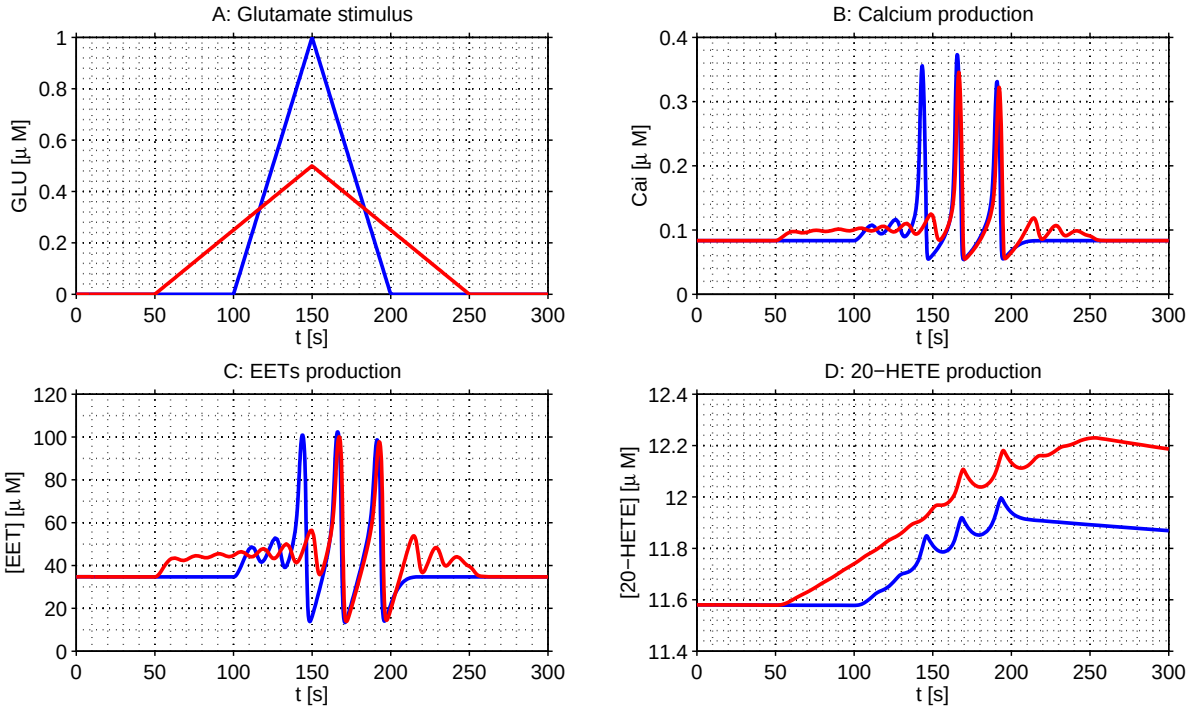

Figure 4.3: Response of an astrocyte to different triangular glutamate stimuli. The blue line represents the response to the stimulus in $t \in [100, 200]s$ with peak $S = 1\mu M$, the red line represents the response to the stimulus in $t \in [50, 250]s$ with peak $S = 0.5\mu M$. The glutamate concentration (panel A), the calcium concentration (panel B), the EETs concentration (panel C) and the 20-HETE concentration (panel D) are shown.

levels. The GLU concentration is different from zero in $t \in (100, 200)s$ and the peaks in GLU stimuli are $S = 1\mu M$, $S = 0.4\mu M$, $S = 0.07\mu M$ for the blue, red and green line, respectively. The behavior is similar to the response to the step stimuli: high GLU levels cause sustained oscillations in calcium and EETs concentration. Moreover, the response of 20-HETE is slower than EETs and does not reach an equilibrium value during the stimulation time.

Figure 4.3 compares the results obtained by applying three different triangular stimuli for the same observational time of $300s$. The total amount of applied GLU is constant, but the application time and the peak of the stimuli are different. In particular, the blue line represents the response to the stimulus in $t \in [100, 200]s$ with a peak $S = 1\mu M$, the red line represents the response to the stimulus in

Parameter	Value	Description
$[IP_3^*]$	0.16 μM	Steady-state concentration of IP_3
τ_r	7.14 s	Loss constant for $[IP_3]$
k_g	0.78 μM	Glutamate stimulation of IP_3
p	0.3	Hill coefficient for IP_3 production via glutamate
α	0.8	Relative wighting of the two IP_3 production pathways
k_4	1.1 μM	Disassociation constant for calcium stimulation of IP_3
Ca_t	2.0 μM	Total calcium concentration in an astrocyte
B_T	10 μM	Total buffer concentration
K_D	20 μM	Buffer disassociation constant
c_1	0.185	Ratio of ER volume/ cytosolic volume
v_1	$6.0 s^{-1}$	Maximum calcium channel flux (ER to cytosol)
v_2	0.11 s^{-1}	Calcium leak constant (ER to cytosol)
v_3	2.2 $\mu M s^{-1}$	Max calcium pump capacity (cytosol to ER)
v_4	0.5 $\mu M s^{-1}$	Max production rate of IP_3
v_g	0.062 $\mu M s^{-1}$	Rate of IP_3 production by glutamate
k_3	0.1 μM	Half-saturation point for calcium pump
a_2	0.14 $\mu M^{-1} s^{-1}$	Calcium inhibition constant
d_1	0.13 μM	IP_3 disassociation constant
d_2	1.049 μM	Disassociation constant for calcium inhibition
d_3	0.9434 μM	Disassociation constant for IP_3
d_5	0.082 μM	Calcium activation constant
AA_b	9.3 μM	Baseline AA concentration
AA_{max}	29.0 μM	Max increase in AA concentration above baseline
AA_M	0.161 μM	Michaelis-like constant for AA production
V_{A11}	0.212 $\mu M s^{-1}$	Maximum 20-HETE production rate (CYP4A11)
K_{A11}	228.2 μM	Michaelis constant of 20-HETE production (CYP4A11)
V_{F2}	0.0319 $\mu M s^{-1}$	Maximum 20-HETE production rate (CYP4F2)
K_{F2}	23.5 μM	Michaelis constant of 20-HETE production (CYP4F2)
λ	0.0015 s^{-1}	Exponential decay rate for 20-HETE
τ_{EET}	0.606 s	Characteristic time for EETs production
k_{EET}	3.73	EETs prouction coefficient

Table 4.1: Summary of parameters for the astrocyte model (values taken as in [12])

$t \in [50, 250]s$ with a peak $S = 0.5\mu M$. Similar responses in calcium and EETs are observed in both cases. Even though the oscillations start at different time instants, the amplitude of the oscillations and the magnitude of the equilibrium state before the oscillations almost coincide. The behavior of 20-HETE seems, instead, to be different. We can notice the same delay in the oscillations onset as for calcium and EETs, but 20-HETE never reaches an equilibrium value, since the magnitude of the concentration is larger for the longer stimuli.

These three sets of simulations highlight the following important facts:

- the calcium oscillation that experiments report can be reproduced;
- the different time scale of EETs and 20-HETE can be reproduced, and the behavior of 20-HETE is qualitatively different from that of EETs;
- the choice of the stimulus is crucial for quantitative considerations.

These facts show that the model can account for many experimental observations, despite the number of introduced simplifications.

4.2 Vascular model

The model presented in section 2.2.2 has been solved using the values of the parameters indicated in [16] and reported in table 4.2.
The baseline condition is defined as the steady state in the absence of radius variation ($\eta_b = 0$, where the subscript b indicates baseline quantities), and it is used to set the initial condition for the model variables. Equations (2.18), (2.20), (2.21) and (2.24) can be easily solved analitically at the stady state. Starting from equation (2.24a) and using $\eta_b = 0$, it follows that

$$f_b = \frac{P_0 R_0}{h_0 k_2}. \tag{4.1}$$

Using the above espression for f_b and setting the time derivative equal to zero in equation (2.21), we obtain:

$$C_b = \frac{\alpha_2 f_b}{\gamma} + C_{th} \tag{4.2}$$

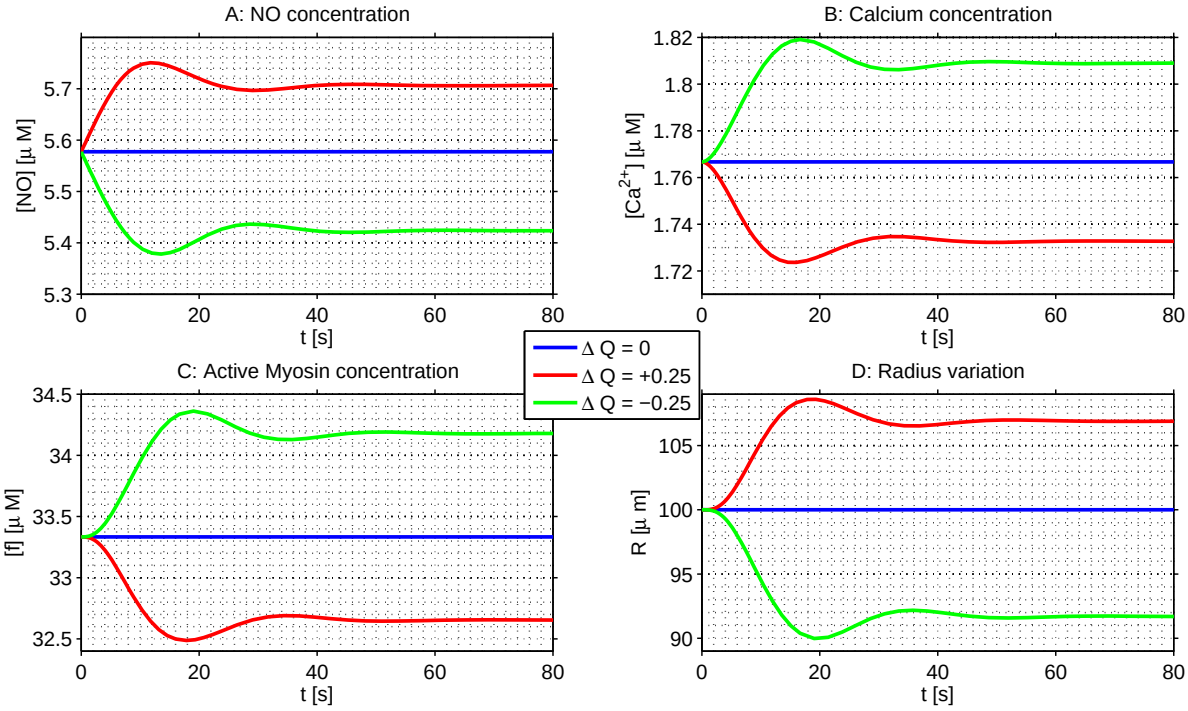

Figure 4.4: Response of an infinitesimal wall portion to different ΔQ. The blue line is the baseline, the red line is the response to an increase in the average blood-flow rate by 25%, the green line is the response to a decrease in the average blood-flow rate by 25%. The NO concentration (panel A), the calcium concentration (panel B), the active myosin concentration (panel C) and the radius variation (panel D) are shown.

and substituiting in equation (2.20a) yields:

$$n_b = \frac{\phi_0 - \alpha_1 C_b}{k_1 C_b}. \tag{4.3}$$

Finally, using equation (2.18a), we can find ψ_0 (equivalent to τ_0) as:

$$\psi_0 = k_e n_b. \tag{4.4}$$

The main mechanisms we want to investigate are:

1. the response of the system to a change in blood flow;

2. the stability of the system when initial conditions differ from equilibrium.

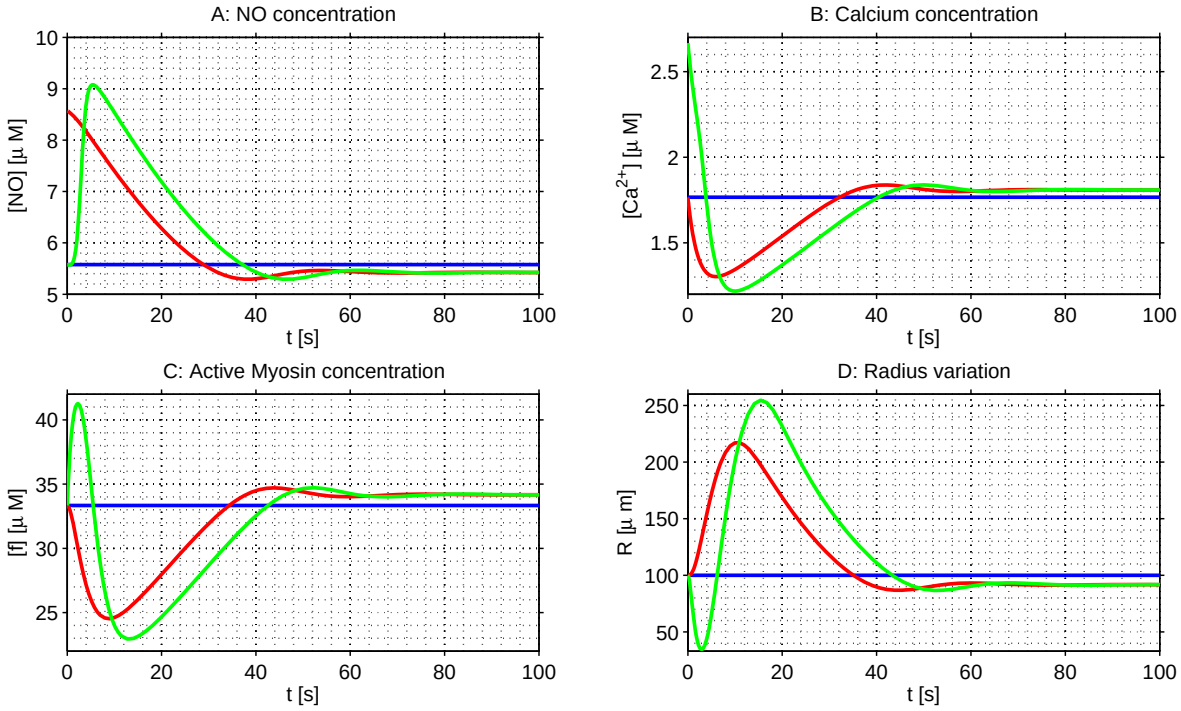

Figure 4.5: Response of an infinitesimal wall portion to different initial condition. The blue line is the baseline, the red line is the response to an increase in the NO initial concentration, the green line is the response to an increase in calcium initial concentration. The NO concentration (panel A), the calcium concentration (panel B), the active myosin concentration (panel C) and the radius variation (panel D) are shown.

The simulation results pertaining to point 1 are reported in figure 4.4. The blue line is the baseline, the red and green line are the responses of the system to an increase or a decrease in the average blood-flow rate by 25%, respectively. We can notice that an increase in blood flow, that is assocated with an increase in shear stress, causes the production of NO. Then, after the cascade of chemical reactions illustrated in figures 2.8 and 2.9, the dilation of the vessel occurs, as expected from experimental obervations [16]. If blood flow decreases, an equivalent phenomenon is observed, even though not symmetric: the decrease in the shear stress causes the consumption of NO and then the constriction of the vessel.

The simulation results pertaining to point 2 are reported in figure: 4.5. The blue line is the baseline, the red line is the response to an increase in the NO

Parameter	Value	Description
R_0	100 μm	Initial lumen radius
h_0	30 μm	Initial wall thickness
k_e	0.0179 s^{-1}	Characteristic of NO transfer from cell into blood flow
psi_0	0.0998 $\mu M s^{-1}$	Source term equivalent to τ_0
α_1	0.05 s^{-1}	Coefficient of NO-independent active Ca^{2+}
k_1	0.05 $\mu M^{-1} s^{-1}$	Coefficient of NO-mediated decrease in intracellular Ca^{2+}
ϕ_0	0.581 μM	Source term equivalent to difference beetwen C_e and C
α_2	0.5 s^{-1}	Dephosphorylation rate coefficient
γ	10 s^{-1}	Phosphorylation rate coefficient
C_{th}	0.1 μM	Threshold concentration of specific myosin-activating ferments
P_0	$2 * 10^4 Pa$	Transmural pressure
λ	150 $Pa\ \mu m^{-1} s$	Viscosity coefficient of the arterial wall
E_0	$0.15 * 10^5\ Pa$	Young's modulus of the arterial wall at the stationary state
κ_1	0.2250	Non-linear elasticity coefficient of the arterial wall
k_2	2000 $Pa\ \mu M^{-1}$	Coefficient of proportionality of the muscular tonus response to the phosphorylated myosin concentration
ε	0.1	Coefficient of proportionality of the Young's modulus response to the phosphorylated myosin concentration
ξ	0.5	Poisson's ratio of the arterial wall

Table 4.2: Summary of parameters for the vascular model (values taken as in [16])

initial concentration and the green line is the response to an increase in calcium initial concentration. The system is stable with respect to such a perturbation from the baseline condition. As a matter of fact, after oscillations of few seconds, the quantities return close to the baseline. This stability shows that the system is able to respond even under extreme working conditions which are represented by non physiological concentration of the chemical agents that may indicate pathological conditions.

4.3 Neurovascular coupling model

The model presented in section 2.3.1 has been solved using the parameter values reported in tables 4.1 and 4.2.
The aims of these simulations are:

1. to calibrate the parameters in such a way that they are consistent with experiments in a healthy state situation;
2. to test if the model can reproduce some experimental observations, including vessel vasodilation during the stimulus and return to baseline after the stimulus is switched off;
3. to identify differences in the vessel response to different glutamate stimuli.

The baseline condition is defined as the steady state in the absence of radius variation ($\eta_b = 0$) and glutamate input, and it is used to set the initial conditions for model variables. The astrocyte block of the system can be solved offline. It is not different from the case previously studied. The vascular block includes three new parameters $\tilde{\alpha}_1$, k_1^E and k_1^H, so that we want to calibrate them in such a way that the baseline conditions are the same as in the previous case. In particular we want η_b to be equal to zero, and ψ_0 to be equal to the previous value. Using the same procedure as in section 4.2 we find:

$$\tilde{\alpha}_1 = \alpha_1 \tag{4.5a}$$

$$k_1^E [EET]_b C_b = k_1^H [20 - HETE]_b C_b \,. \tag{4.5b}$$

So if we fix k_1^E, for example, all the other parameters are known.

The first simulation, represented in figure 4.6, verifies the parameter calibration and the correct behavior of the system. The blue line is the baseline value, the other lines are the result of the simulation for different values of k_1^H, having set $k_1^E = 0.0016 \mu M^{-1} s^{-1}$ and applying the stimulus in panel A. The red line is calculated using the parameter k_1^H found with equation (4.5b); we can verify that the baseline value is the desired one. Using a low value for k_1^H causes a pathological vasodilation, while using a high value of k_1^H causes a pathological vasoconstriction, as expected.

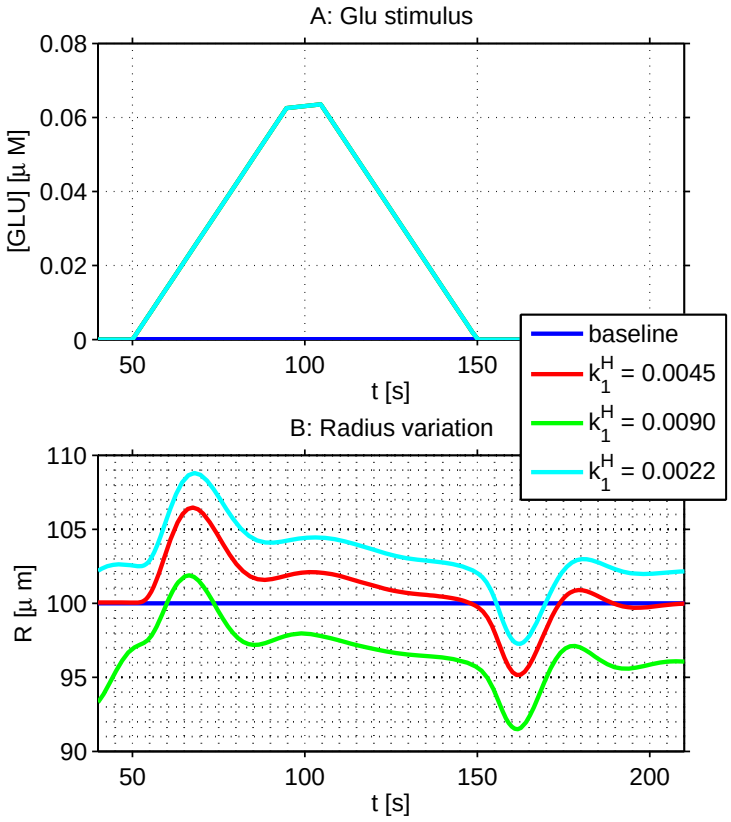

Figure 4.6: Response of the wall section to the glutamate stimulus represented in panel A, with $\Delta Q = 0$. The blue line is the baseline, the other lines use $k_1^E = 0.0016 \mu M^{-1} s^{-1}$ and k_1^H as in the legend, expressed in $\mu M^{-1} s^{-1}$. The red line corresponds to the correct calibration of the parameters according to (4.5b). The glutamate concentration (panel A) and the radius variation (panel B) are shown.

The changes in k_1^H may help simulate pathological conditions such as vasospasm. The general behavior agrees with the experimental results: we can see vasodilation while the glutamate stimulus is active, and a vasoconstriction that permits the return to the baseline condition when the stimulus is switched off.

The second simulation is illustrated in figure 4.7. The blue line represents the baseline, the red line represents the response to a triangular stimulus, and the green line represents the response to a step stimulus. The total glutamate that reaches the astrocyte is the same in both cases and the parameters are chosen according to equation (4.5b). The responses to the stimuli are comparable, but we can notice

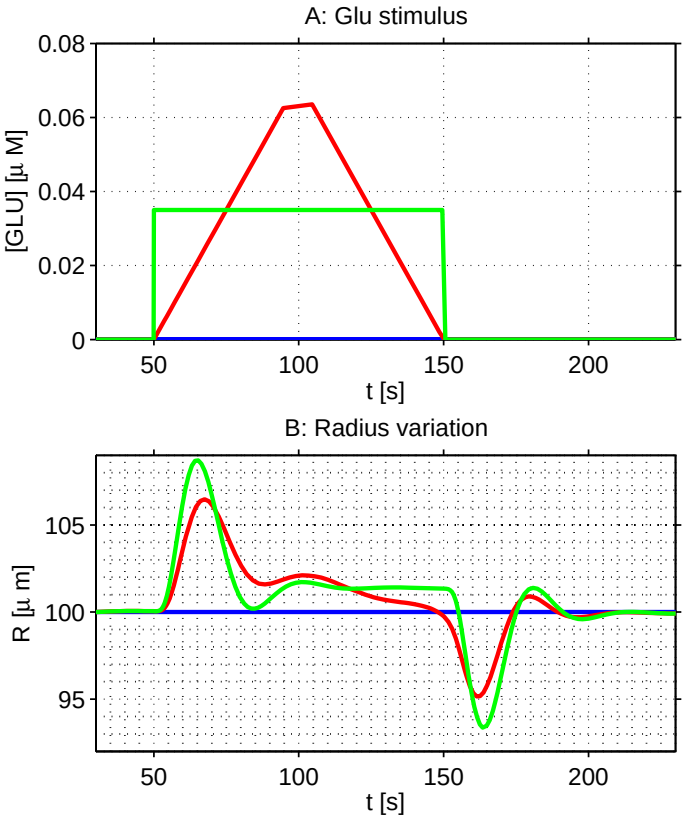

Figure 4.7: Response of the wall section to the glutamate stimuli represented in panel A with $\Delta Q = 0$. The blue line is the baseline, the red line is the response to a triangular stimulus, the green line is the response to a step stimulus. The glutamate concentration (panel A) and the radius variation (panel B) are shown.

that the oscillations at the beginning and at the end of the stimulus are much more marked in the step case. Moreover, the vasodilation during the stimulus is more regular in the step case than in the triangular case. These results confirm the importance of choosing the correct shape of the input stimulus. It is not easy to tell which shape is more realistic for the glutamate input; regardless, it is interesting to notice that the qualitative behavior of the system does not exhibit a substantial variation under different input triggering signals.

Based upon the previous simulation results, we proceed to validate the models by verifying that their predictions are in agreement with experimental observations. The main challenge in studying the models presented in sections 2.1.3, 2.2.2 and

Parameter	LA	SA	C	SV	LV
Steady state diameter $2R_0$, μm	105.0	47.2	6.0	68.5	154.9
No. of segments, N	4	40	187,890	40	4
Segment length, L, cm	0.73	0.52	0.067	0.52	0.73
Viscosity, μ, cP	2.28	2.06	10.01	2.09	2.44
Capacitance Cap, $ml/mmHg$	$7.53 \cdot 10^{-7}$	$7.53 \cdot 10^{-7}$		$1.67 \cdot 10^{-5}$	$1.67 \cdot 10^{-5}$

Table 4.3: Summary of parameters for the neurovascular coupling model for retinal microcirculation (values taken as in [2, 10])

2.3.1 is that it is not easy to obtain *in vivo* measurements of the quantities that we use as input, output and model parameters.

4.4 Neurovascular coupling model for retinal microcirculation

The model presented in section 3.4 has been solved using the values of the parameters adopted in [2, 10, 16, 12] and reported in tables 4.1, 4.2 and 4.3. In particular, for the astrocyte block of the system the values in table 4.1 are used. For the electrical block of the system the values in table 4.3 are used, with $P_{in} = 25mmHg$, so that the pressure drop across the vessel network is constant: $\Delta P = 25mmHg$. For the vascular block the parameters in table 4.2 are used with $R_0^{LA} = 52.5\mu m$, $R_0^{SA} = 23.6\mu m$ as in table 4.3. The wall thickness is chosen such that the ratio $\frac{R_0^{(m)}}{h_0^{(m)}}$, $m = LA, SA$ is mantained constant, consistently with the observation that the SMCs layers decrease as vessels become smaller. Therefore $h_0^{LA} = 13.125\mu m$ and $h_0^{SA} = 5.9\mu m$.

The baseline condition is defined as the steady state in the absence of radius variation ($\eta_b^{(m)} = 0$, $m = LA, SA$) and glutamate input ($S^{(m)} = 0$, $m = LA, SA$). The baseline values are found numerically and they are used to set the initial conditions for the following simulations.

The first simulation studies the response of the system when the same GLU

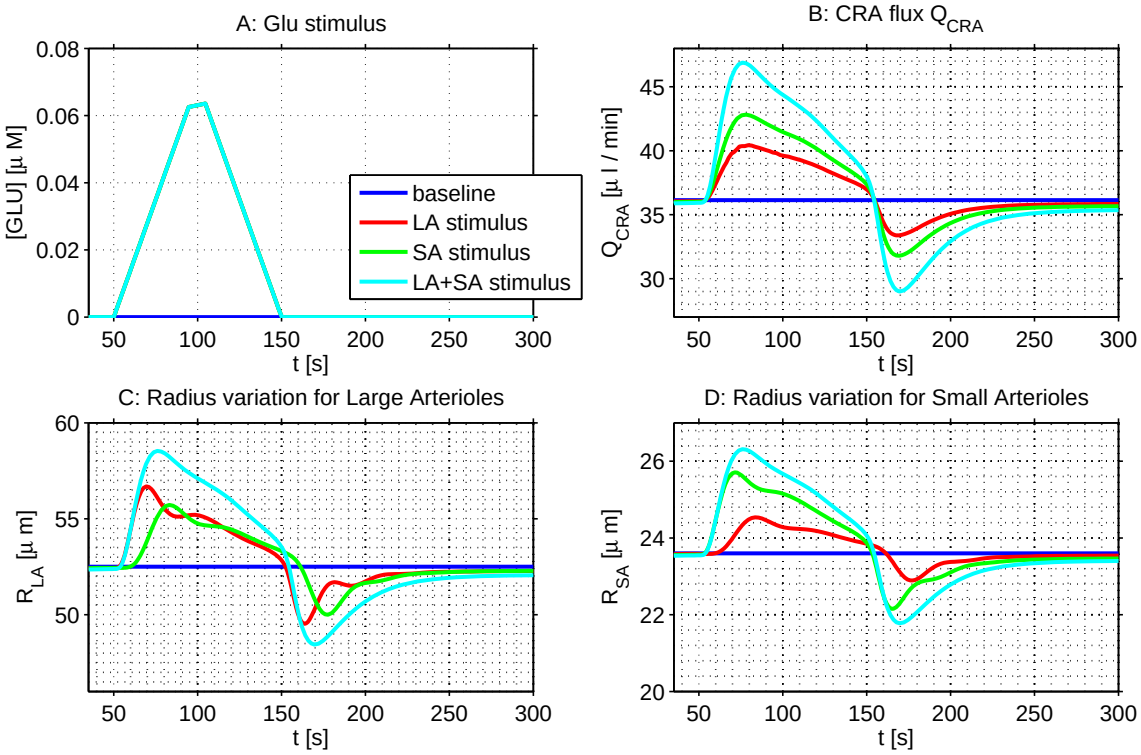

Figure 4.8: Results for the NVC model for retinal microcirculation with the same GLU input applied on different compartments. The blue line is the baseline condition, the red line is the response of the system when the stimulus is applied only to the LA compartment, the green line is the response of the system when the stimulus is applied only to the SA compartment, the cyan line is the response of the system when the stimulus is applied to both vasoactive compartments. The GLU stimulus (panel A), the CRA flux (panel B), the radius variation for large (panel C) and small (panel D) arterioles are shown.

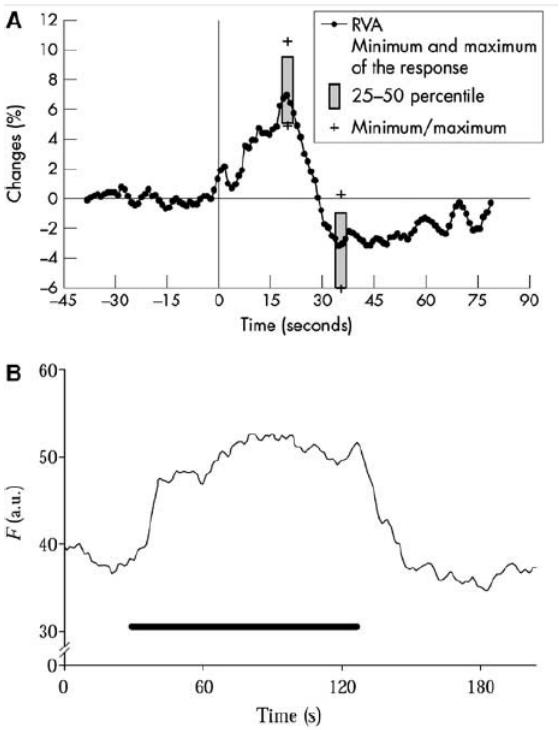

Figure 4.9: The functional hyperemia response in the retina. Panel A: change % in mean arterial diameter using 20s of luminance flicker, as measured by retinal vessel analyzer in five subjects. The stimulus started at time 0. Panel B: blood flow increase to flicker stimulation (black bar) measured at the rim of the optic disk in cats with laser Doppler flowmetry. Reprinted from [24]

stimulus is applied to different compartments. The results are represented in figure 4.8: the blue line is the baseline condition; the red line is the response of the system when the stimulus is applied only to the LA compartment; the green line is the response of the system when the stimulus is applied only to the SA compartment; the cyan line is the response of the system when the stimulus is applied to both vasoactive compartments. We can notice that the response in terms of vasodilation-vasoconstriction starts with a delay of a few seconds in the compartment where the stimulus has been applied. Regardless of where the stimulus is applied, both LA and SA compartments exhibit a vasodilation response, even though on different time scales; the vasodilation is mediated by flux and shear stess changes. Moreover these results suggest that a stimulus applied on the SA compartment has a greater effect than a stimulus applied on the LA compartment. Obviously, when the stimulus is applied to both vasoactive compartments, the flux response is stronger than in the

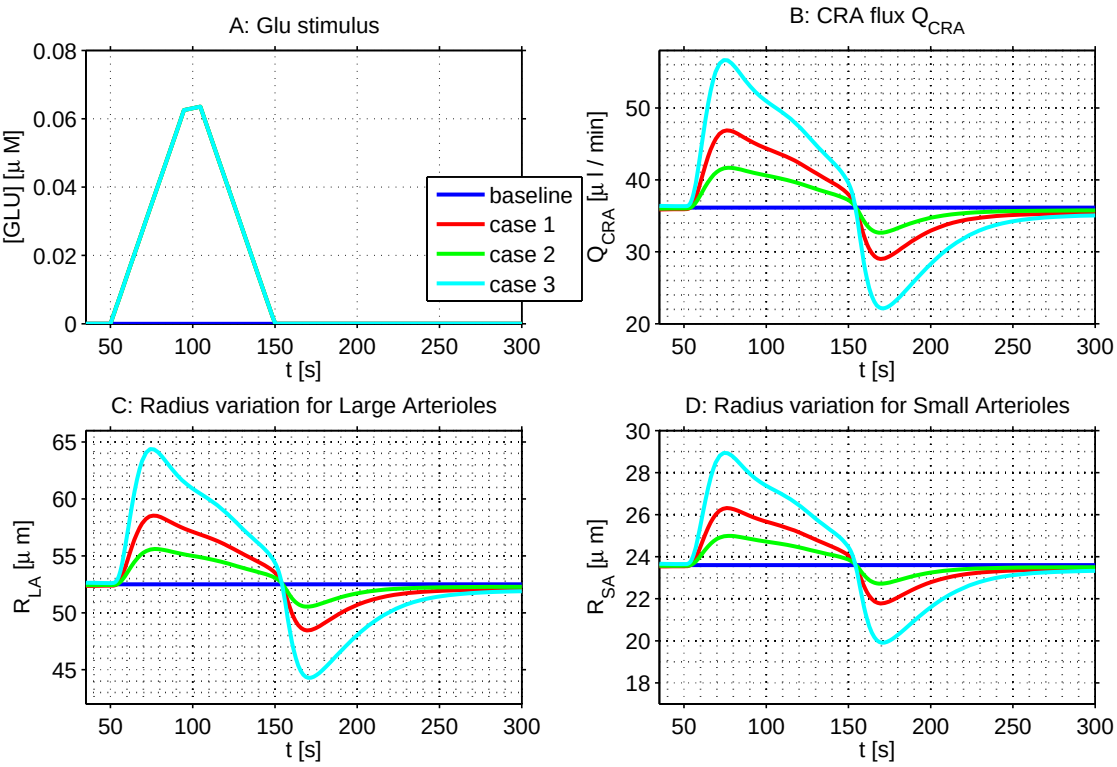

Figure 4.10: Results for the NVC model for retinal microcirculation with different parameters. The blue line is the baseline condition. The other lines are the response to the same glutamate stimulus applied on both the LA and SA compartments, but using different parameters. Case 1 (red line) uses $k_1^E = 0.0016\mu M^{-1}s^{-1}$ and $k_1^H = 0.0046\mu M^{-1}s^{-1}$. Case 2 (green line) uses $k_1^E = 0.0008\mu M^{-1}s^{-1}$ and $k_1^H = 0.0023\mu M^{-1}s^{-1}$. Case 3 (cyan line) uses $k_1^E = 0.0032\mu M^{-1}s^{-1}$ and $k_1^H = 0.0091\mu M^{-1}s^{-1}$. The glutamate stimulus (panel A), the CRA flux (panel B), the radius variation for large (panel C) and small (panel D) arterioles are shown.

previous separate cases.

The model simulations also provide a reasonable baseline value for retinal blood flow. Experimental values for CRA blood flow rates in humans range between $30\mu l/min$ and $38\mu l/min$ for healthy subjects [26] (fig: 4.9, panel B). This value is in agreement with the baseline value of $36\mu l/min$ obtained from the simulation (see figure 4.8, panel B). The simulation results are also consistent with experimental findings related to flicker stimulation. Several studies reported vessel dilation (up to approximately 8%) during a flicker stimulation and a transient vasocostriction (up to approximately 4%) at the end of the stimulus [26, 24] (see figure 4.9, panel A). This is consistent with our results (see figure: 4.8). Other studies also report a

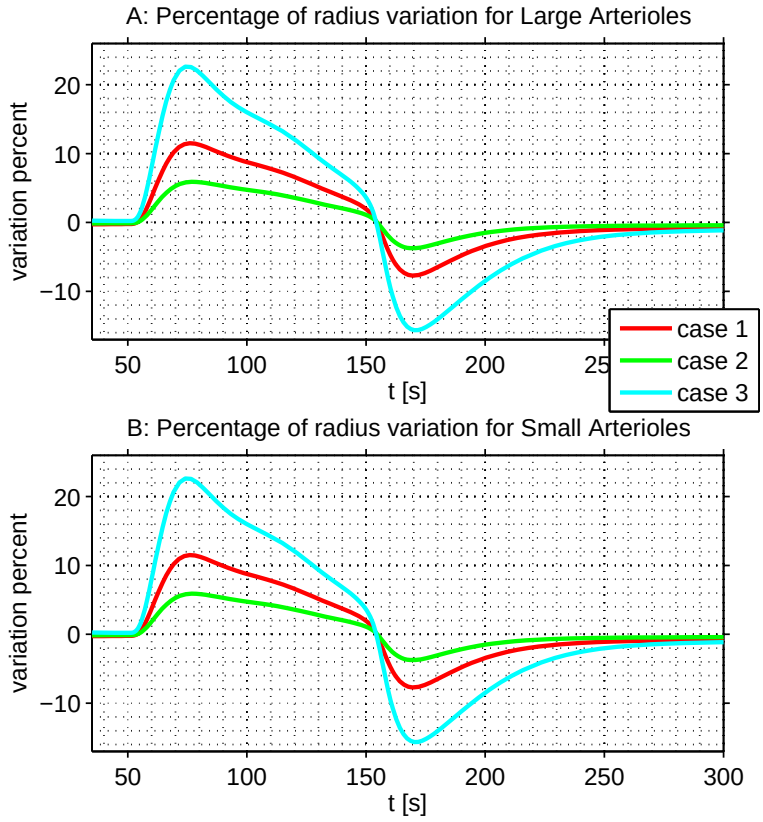

Figure 4.11: Percentage of radius variation for the simulation in figure 4.10. Panel A: variation for large arterioles, panel B: variation for small arterioles

blood flow increase of approximately $30 - 38\%$ at the CRA level [24]. Our results are in good agreement with this experimental evidence, see figures 4.9, panel B and 4.8, panel B.

The second simulation studies the importance of choosing the correct model parameters, particularly for k_1^E and k_1^H as in equation (4.5b). The results are presented in figure 4.10: the same glutamate stimulus is applied on both LA and SA compartments. Case 1 (red line) uses $k_1^E = 0.0016\mu M^{-1}s^{-1}$ and $k_1^H = 0.0046\mu M^{-1}s^{-1}$. Case 2 (green line) uses $k_1^E = 0.0008\mu M^{-1}s^{-1}$ and $k_1^H = 0.0023\mu M^{-1}s^{-1}$. Case 3 (cyan line) uses $k_1^E = 0.0032\mu M^{-1}s^{-1}$ and $k_1^H = 0.0091\mu M^{-1}s^{-1}$. The various results are qualitatively comparable, but the magnitude of the changes is different. If we compare these results with experimental data ([24, 26], figure 4.9, panel A) it turns out that case 1 and case 2 are reasonable, while case 3 seems to exhibit

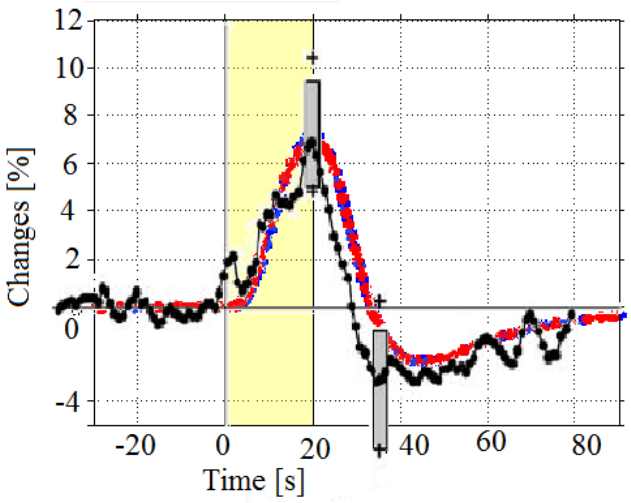

Figure 4.12: Percentage of radius variation for the simulation versus experimental results. The black line represents the experimental result already shown figure 4.9. The blue and red lines are the percentage radius variations in LA and SA compartments, respectively. The stimulus is applied for $t \in [0, 20]s$, and a triangular GLU shape with peak $0.07\mu M$ is chosen for the numerical simulation. $k_1^E = 0.0008\mu M^{-1}s^{-1}$ and $k_1^H = 0.0023\mu M^{-1}s^{-1}$ are used.

too much vasodilation. However also the choice of the stimulus can influence the magnitude of the response, so a careful balance of all the mechanisms is in order.

Figure 4.11 shows a detail of the percentage radius variation for small and large arterioles. We can notice that the percentage variation is the same in both cases. This is caused by the choice of parameters, that are the same in both cases and the ratio $\frac{R_0^{(m)}}{h_0^{(m)}}$, $m = LA, SA$ is mantained constant. Different results can be obtained with different parameters or different stimuli in the compartments. In figure 4.12 a comparison between experimental (panel A figure 4.9) and simulated data is reported. In particular the stimulus is applied for $t \in [0, 20]s$ in both cases. A triangular GLU shaped input with peak $0.07\mu M$, $k_1^E = 0.0008\mu M^{-1}s^{-1}$ and $k_1^H = 0.0023\mu M^{-1}s^{-1}$ are chosen for the numerical simulation. We can notice that the simulation is in excellent agreement with the experimentally measured radius dynamics both in time scale and magnitude of the variation.

The last simulation examines the response to different glutamate stimuli applied on both the vasoactive compartments. The results are shown in figure 4.13: the blue

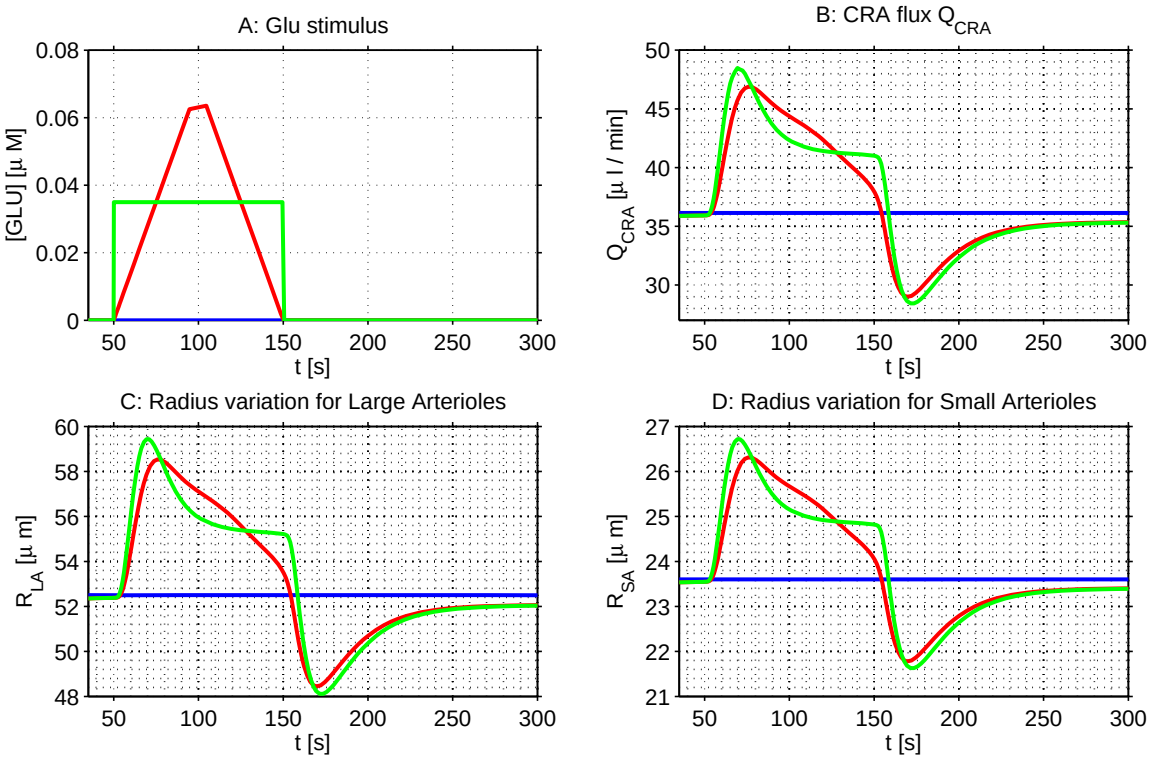

Figure 4.13: Results for the NVC model for retinal microcirculation with different glutamate input shape. The blue line is the baseline solution, the red line is the response to a triangular stimulus, the green line is the response to a step stimulus. The glutamate stimulus (panel A), the CRA flux (panel B), the radius variation for large (panel C) and small (panel D) arterioles are shown.

line is the baseline solution, the red line is the response to a triangular stimulus, the green line is the response to a step stimulus. The total amount of glutamate applied is the same in all cases. The magnitudes of the changes in vessel diameter and flow are comparable, but the qualitative behavior is a little bit different. The triangular stimulus leads to a more regular solution, whereas the step stimulus leads to an initial peak of the solution and then to a plateau before vasoconstriction occurs.

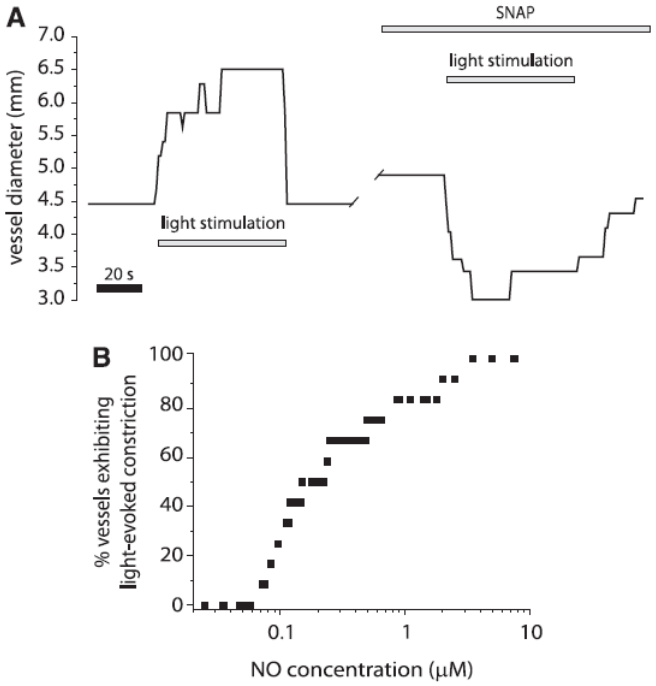

Figure 4.14: NO depresses light-induced vasodilation and unmask vasoconstriction in the retina. Panel A: flicker stimulation evokes arteriole dilation in *ex vivo* whole-mount rat retina. When NO levels are raised by the addition of an NO donor (SNAP), the vasodilation is depressed, revealing a flicker-induced vasoconstriction. Panel B: When NO concentration is low, flicker evokes vasodilation, but not vasoconstrictions; as NO levels are raised, the fraction of vessels displaying vasoconstrictions increases. Reprinted from [24]

4.5 Neurovascular coupling model for retinal microcirculation with impaired neural NO production

The model presented in section 3.5 has been solved using the same parameter values used in section 4.4. The new model parameters are $[nNO]$, δ and β and a set of simulations is conducted to verify the impact of such parameters on the solution. The baseline condition is defined as the steady state in the absence of radius variation ($\eta_b^{(m)} = 0,\ m = LA, SA$), glutamate input ($S^{(m)} = 0,\ m = LA, SA$) and $[nNO]$ input, so that it is the same as in section 4.4.

The experimental results for the pathological conditions in the case of rat retina are shown in figure 4.14: the healthy situation exhibits vasodilation during the stimulus (panel A, on the left), while the situation with forced production

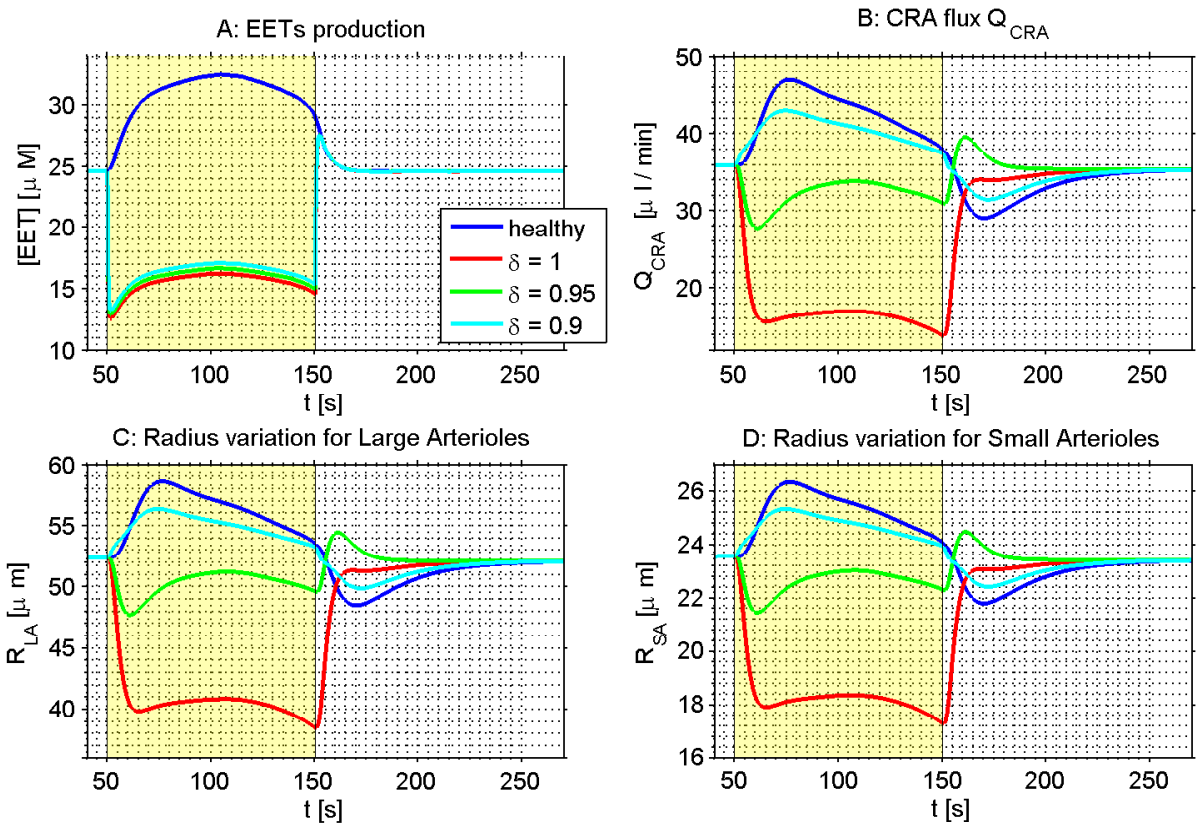

Figure 4.15: Results for the NVC model for retinal microcirculation with impaired nNO production using different values of δ and the same triangular glutamate input applied from 50 to 150s, with a peak of 0.07μM. For every case $\beta = 0.25$ and $[nNO] = [nNO]_b$ for $t < 50s$ and $t > 150s$, $[nNO] = 5\mu M$ for $50s \leq t \leq 150s$. The blue line is the healthy condition, the red line uses $\delta = 1$, the green line uses $\delta = 0.95$, the cyan line uses $\delta = 0.9$. The yellow area is the time when glutamate and $[nNO]$ input are active. The EETs concentration (panel A), the CRA flux (panel B), the radius variation for large (panel C) and small (panel D) arterioles are shown.

of nNO exhibits vasoconstriction during the stimulus (panel A, on the right). Varying the forced nNO level, different results are produced (panel B): when $[nNO] \ll [nNO]_b \simeq 1\mu M$ only vasodilation occurs, when $[nNO] \gg [nNO]_b$ only vasoconstriction occurs [24, 22].

In figure 4.15 the results of the simulation with different values of δ are shown. The same triangular glutamate input is applied from 50 to 150s, with a peak of 0.07μM. For every case $\beta = 0.25$ and $[nNO] = [nNO]_b$ for $t < 50s$ and $t > 150s$, $[nNO] = 5\mu M$ for $50s \leq t \leq 150s$. The blue line is the healthy condition, the red

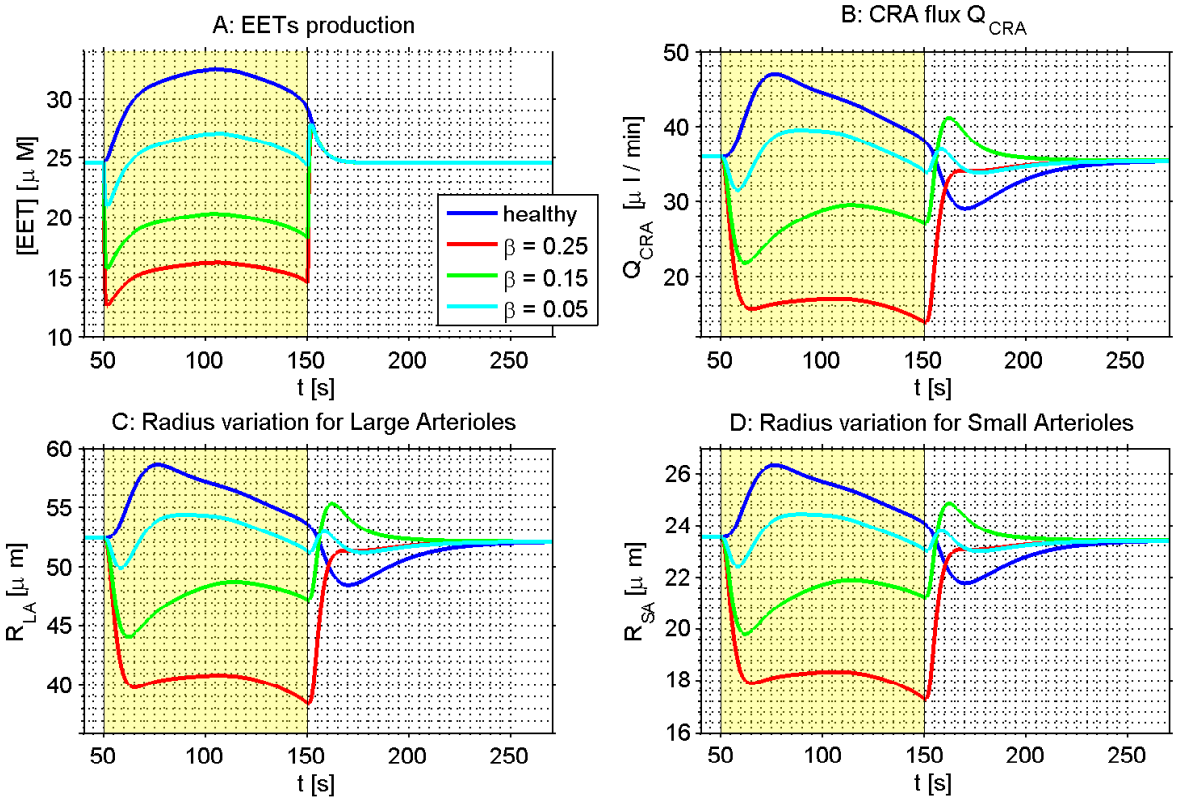

Figure 4.16: Results for the NVC model for retinal microcirculation with impaired nNO production using different values of β and the same triangular glutamate input applied from 50 to 150s, with a peak of 0.07μM. For every case $\delta = 1$ and $[nNO] = [nNO]_b$ for $t < 50s$ and $t > 150s$, $[nNO] = 5\mu M$ for $50s \leq t \leq 150s$. The blue line is the healthy condition, the red line uses $\beta = 0.25$, the green line uses $\beta = 0.15$, the cyan line uses $\beta = 0.05$. The yellow area is the time when glutamate and $[nNO]$ input are active. The EETs concentration (panel A), the CRA flux (panel B), the radius variation for large (panel C) and small (panel D) arterioles are shown.

line uses $\delta = 1$, the green line uses $\delta = 0.95$, the cyan line uses $\delta = 0.9$. We can see that if $[nNO]$ reaches the SMCs it exerts a great vasodilating effect, while if $[nNO]$ reaches only the astrocyte ($\delta = 1$) the pathological effect occurs. Moreover with $\delta = 1$ the percentage vasoconstriction of the vessels is about 30% in agreement with the experimental results (figure 4.14, panel A, SNAP case).

In figure 4.16 the results of the simulation with different values of β are shown. The same triangular glutamate input is applied from 50 to 150s, with a peak of 0.07μM. For every case $\delta = 1$ and $[nNO] = [nNO]_b$ for $t < 50s$ and $t > 150s$,

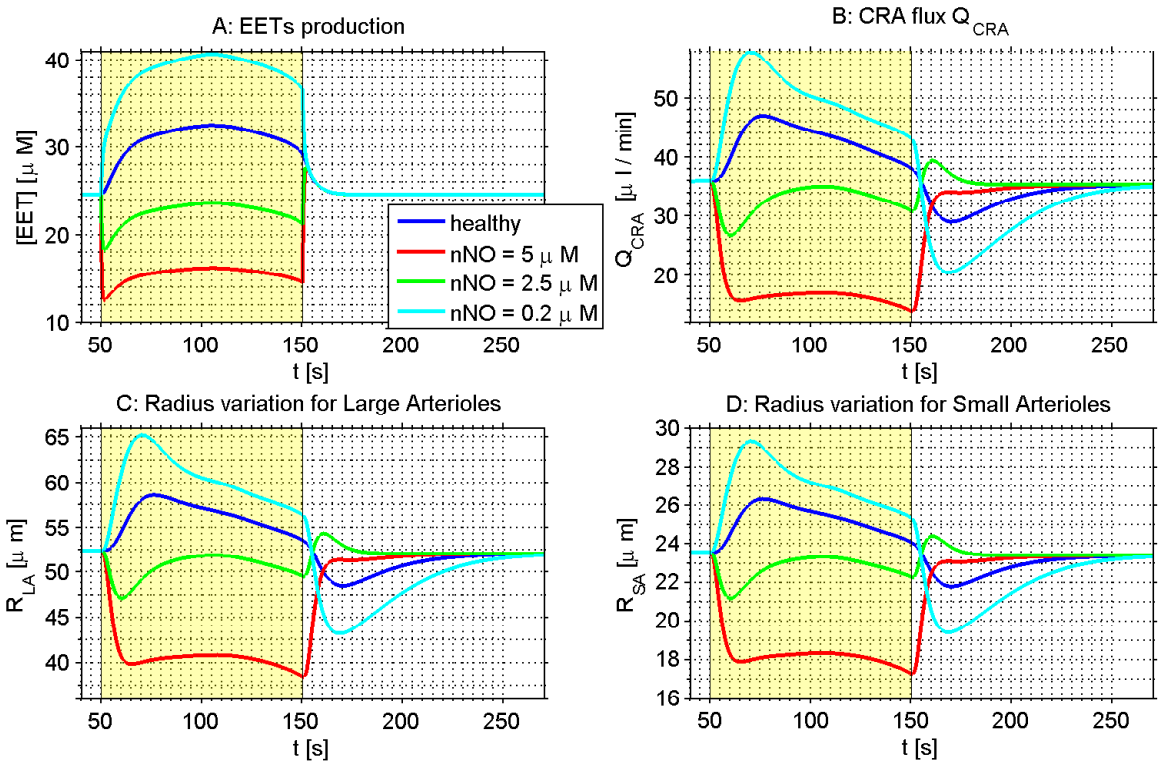

Figure 4.17: Results for the NVC model for retinal microcirculation with impaired nNO production using different $[nNO]$ as input and the same triangular glutamate stimulus applied from 50 to 150s, with a peak of 0.07μM. For every case $\delta = 1$, $\beta = 0.25$ and $[nNO] = [nNO]_b$ for $t < 50s$ and $t > 150s$. The blue line is the healthy condition, the red line uses $[nNO] = 5\mu M$ for $50s \leq t \leq 150s$, the green line uses $[nNO] = 2.5\mu M$ for $50s \leq t \leq 150s$, the cyan line uses $[nNO] = 0.2\mu M$ for $50s \leq t \leq 150s$. The yellow area is the time when glutamate and $[nNO]$ input are active. The EETs concentration (panel A), the CRA flux (panel B), the radius variation for large (panel C) and small (panel D) arterioles are shown.

$[nNO] = 5\mu M$ for $50s \leq t \leq 150s$. The blue line is the healthy condition, the red line uses $\beta = 0.25$, the green line uses $\beta = 0.15$, the cyan line uses $\beta = 0.05$. The parameter β provides a measure of the effectiveness of the overproduction of $[nNO]$. Lowering the value of β leads to a decrease in the pathological effect, whereas increasing the value of β enhances vasoconstriction.

The last simulation results are reported in figure 4.17, where the influence of different $[nNO]$ inputs is investigated. The same triangular glutamate stimulus is applied from 50 to 150s, with a peak of 0.07μM. For every case $\delta = 1$, $\beta = 0.25$ and

$[nNO] = [nNO]_b$ for $t < 50s$ and $t > 150s$. The blue line is the healthy condition, the red line uses $[nNO] = 5\mu M$ for $50s \leq t \leq 150s$, the green line uses $[nNO] = 2.5\mu M$ for $50s \leq t \leq 150s$, the cyan line uses $[nNO] = 0.2\mu M$ for $50s \leq t \leq 150s$. We can notice that elevated $[nNO]$ results in a marked vasoconstriction, that is less evident when $[nNO]$ is decreased. Moreover when $[nNO] < [nNO]_b$ no vasoconstriction occurs, but the vasodilation is increased, consistently with the experimental results ([24], figure: 4.14, panel B). Obviously the present model is based on lumped parameters, and all the vessels in the compartment exhibit the same behavior. Nevertheless it is significant that the response of the model to the medium-size values of $[nNO]$ is intermediate between the marked vasoconstriction and vasodilation.

Conclusions and Future Perspective

In this work of thesis a novel model for the description of NVC mechanism is proposed. Our description relies on the models presented in [12, 16] to perform the coupling between the mechanical behavior of the vessel and the vasoactive response due to NVC. The novel approach is a local description based on an ODEs system which

1. neglects the spatial distribution of the various cell types involved in the problem and
2. exploits the representative segment model applied to retinal microcirculation presented in [2].

Through a suitable upscaling of the local NVC model it has been possible to construct a model of the complex retinal vessel network that takes into account the NVC mechanism. Furthermore a new mechanism is added to take into account pathological conditions related to impaired neural NO production.
The obtained numerical results are very promising because they are able to fit experimental observations both qualitatively and quantitatively, despite a number of simplifying assumptions.

Several further studies could extend this work in the future.

- First of all an accurate biological investigation could help better describe the problem. For example capillaries, which are normally assumed to be passive

resistors, may contribute to the regulation of flow in the retina due to the contraction or dilation of pericytes.

- A second extension could be the addition of other regulatory mechanisms such as metabolic feedback, that should take into account the influence of oxygen concentration in the vessel. This exstension would permit to study the relative importance of the single regulatory pathways.

- A third extension could be the modeling of neurons; in particular, it can be helpful to connect a microscale stimulus such as the glutamate concentration with a macroscale stimulus such as the flickering light.

- Finally, higher dimensional models could be used in order to better understand diffusion phenomena in tissues or interactions between nearby cells.

Bibliography

[1] *AGP*. 2014. URL: http://www.altrogiornale.org/comunicazione-astrociti-neuroni/ (cit. on p. 3).

[2] J. Arciero, A. Harris, B. Siesky, A. Amireskandari, V. Gershuny, A. Pickrell, and G. Giudoboni. "Theoretical Analysis of Vascular Regulatory Mechanisms Contributing to Retinal Blood Flow Autoregulation". In: *Invest Ophthalmol Vis Sci. 2013 Aug 19;54(8):5584-93. doi: 10.1167/iovs.12-11543.* (2013) (cit. on pp. vi, viii, xi, 42, 43, 45, 62, 74).

[3] D. Attwell, A. M. Buchan, S. Charpak, M. Lauritzen, B. A. MacVicar, and E. A. Newman. "Glial and neuronal control of brain blood flow". In: *Nature, 468, 232–243, doi:10.1038/nature09613* (2010) (cit. on pp. 2–6, 15–17).

[4] *BWC*. 2015. URL: https://biologywedscomputer.wordpress.com/tag/neuron/ (cit. on p. 4).

[5] R. B. Buxton. *Introduction to functional magnetic resonance imaging*. 2002 (cit. on p. 6).

[6] *eyewiki.org*. 2014. URL: http://eyewiki.aao.org/IOP_and_Tonometry (cit. on p. 11).

[7] W. G. Gibson, L. Farnell, and M. R. Bennett. "A Quantitative Model of Purinergic Junctional Transmission of Calcium Waves in Astrocyte Networs". In: *Biophys J. 2005 Oct; 89(4): 2235–2250.* (2005).

[8] W. G. Gibson, L. Farnell, and M. R. Bennett. "A computational model relating changes in cerebral blood volume to synaptic activity in neurons". In: *Neurocomputing, Volume 70, Issues 10–12, Pages 1674–1679* (2007) (cit. on pp. 17, 29).

[9] W. G. Gibson, G. Lemon, and M. R. Bennett. “Metabotropic receptor activation, desensitization and sequestration-I: modelling calcium and inositol 1,4,5-trisphosphate dynamics following receptor activation”. In: *J Theor Biol. 2003 Jul 7;223(1):93-111.* (2003) (cit. on p. 24).

[10] G. Guidoboni, A. Harris, S. Cassani, J. Arciero, B. Siesky, A. Amireskandari, L. Tobe, P. Egan, I. Januleviciene, and J. Pak. “Intraocular Pressure, Blood Pressure, and Retinal Blood Flow Autoregulation: A Mathematical Model to Clarify Their Relationship and Clinical Relevance”. In: *Invest Ophthalmol Vis Sci. 2014 May 29;55(7):4105-18. doi: 10.1167/iovs.13-13611.* (2014) (cit. on pp. 42–44, 62).

[11] *healthcommunities.com.* 2014. URL: http://www.healthcommunities.com/brain-nerve-tests/transcranial-doppler-ultrasound.shtml (cit. on p. 7).

[12] J. Hadfield, M.l J. Plank, and T. David. “Modeling secondary messenger pathways in neurovascular coupling”. In: *Bull Math Biol. 2013 Mar;75(3):428-43. doi: 10.1007/s11538-013-9813-x.* (2013) (cit. on pp. v, vii, x, 15, 18, 21–23, 25, 26, 50, 54, 62, 74).

[13] K. A. Johnson and R. S. Goody. “The Original Michaelis Constant: Translation of the 1913 Michaelis–Menten Paper”. In: *Biochemistry, 2011, 50 (39), pp 8264–8269* (2011) (cit. on p. 19).

[14] A. Kapela and N. M. Tsoukias. “Multiscale FEM Modeling of Vascular Tone: From Membrane Currents to Vesel Mechanics”. In: *IEEE Trans Biomed Eng. 2011 Dec;58(12):3456-9. doi: 10.1109/TBME.2011.2162513.* (2011).

[15] J. Keener and J. Sneyd. *Mathematical Physiology I: Cellular Physiology.* 2009 (cit. on pp. 17, 19).

[16] N. A. Kudryashov and I. L. Chernyasvskii. “Numerical Simulation of the Process of Autoregulation of the Arterial Blood Flow”. In: *Izvestiya Rossiiskoi Akademii Nauk, Mekhanika Zhidkosti i Gaza, Vol. 43, No. 1, pp. 38–56.* (2008) (cit. on pp. v, vii, x, 16, 27–30, 33, 55, 57, 58, 62, 74).

[17] A. London, I. Benhar, and M.l Schwartsl. “The retina as a window to the brain - from eye research to CNS disrders”. In: *Nat Rev Neurol. 2013 Jan;9(1):44-53. doi: 10.1038/nrneurol.2012.227.* (2013) (cit. on pp. 6–10, 42).

[18] *medlineplus*. 2013. URL: https://www.nlm.nih.gov/medlineplus/ency/article/007341.htm (cit. on p. 7).

[19] *medlineplusIP*. 2013. URL: https://www.nlm.nih.gov/medlineplus/ency/article/003411.htm (cit. on p. 7).

[20] *MTC*. 2000. URL: http://www.perseus.tufts.edu/hopper/text?doc=Perseus:abo:phi,0474,040:18:60 (cit. on p. 7).

[21] F. H. Martini, W. C. Ober, C. W. Garrison, k. W. Welch, R. T. Hutchings, and K. Ireland. *Anatomy and Physiology*. 2007 (cit. on p. 5).

[22] M. R. Metea and E. A. Newman. “Glial Cells Dilate and Constrict Blood Vessels: A Mechanism of Neurovascular Coupling”. In: *J Neurosci. 2006 Mar 15;26(11):2862-70.* (2006) (cit. on pp. xi, 41, 45, 48, 70).

[23] D. Moore, A. Harris, D. WuDunn, N. Kheradiya, and B. Siesky. “Dysfunctional regulation of ocular blood flow: A risk factor for glaucoma?” In: *Clin Ophthalmol. 2008 Dec;2(4):849-61.* (2008) (cit. on pp. 9, 37).

[24] E. A. Newman. “Functional hyperemia and mechanism of neurovascular coupling in the retinal vasculature”. In: *J Cereb Blood Flow Metab. 2013 Nov;33(11):1685-95. doi: 10.1038/jcbfm.2013.145.* (2013) (cit. on pp. xi, 18, 37–41, 48, 64–66, 69, 70, 73).

[25] M. J. Plank, D. J. N. Wall, and T. David. “The role of endothelial calcium and nitric oxide in the localisation of atherosclerosis”. In: *Math Biosci. 2007 May;207(1):26-39.* (2007) (cit. on pp. 16, 31).

[26] C. J. Pournaras, E. Rungger-brändle, C. E. Riva, S. H. Hardarson, and E. Stefansson. “Regulation of retinal blood flow in healt and disease”. In: *Prog Retin Eye Res. 2008 May;27(3):284-330. doi: 10.1016/j.preteyeres.2008.02.002.* (2008) (cit. on pp. 1, 37–43, 65, 66).

[27] D. Prada, A. Harris, G. Guidoboni, B. Siesky, A. M. Huang, and J. Arciero. "Autoregolation and neurovascular coupling in the optic nerve head". In: *Surv Ophthalmol. 2015 Oct 20. pii: S0039-6257(15)00182-4. doi: 10.1016/j.survophthal.2015.10.004.* (2015) (cit. on pp. 2, 3, 10, 11).

[28] L. Siaudvyte, I. Januleviciene, A. Ragauskas, L. Bartusis, B. Siesky, and A. Harris. "Update in intracranial pressure evaluation methods and translaminar pressure gradient role in glaucoma". In: *Acta Ophthalmologica, Volume 93, Issue 1, pages 9–15* (2015) (cit. on p. 7).

[29] *TRE*. 2010. URL: http://www.treccani.it/enciclopedia/glia_%28Dizionario-di-Medicina%29/ (cit. on p. 5).

[30] G. Ullah, P. Jung, and A. H. Cornell-Bell. "Anti-phase calcium oscillations in astrocytes via inositol (1, 4, 5)-trisphosphate regeneration". In: *Cell Calcium. 2006 Mar;39(3):197-208.* (2005).

[31] *fmri*. 2002. URL: http://www.imaging.robarts.ca/~wzheng/Site/fMRI.html.